The explosive engine of the 2022 Hunga submarine eruption

Ryo Okuwaki[1*†], Wenyuan Fan[2†], Osamu Sandanbata[3], Diana C. Roman[4], Yuri Fialko[2]
[1]Institute of Life and Environmental Sciences, University of Tsukuba, Ibaraki, Japan.
[2]Institute of Geophysics and Planetary Physics, Scripps Institution of Oceanography, University of California, San Diego, CA, USA.
[3]Earthquake Research Institute, The University of Tokyo, Tokyo, Japan.
[4]Earth and Planets Laboratory, Carnegie Institution for Science, Washington DC, USA
[*]Corresponding author. Email: rokuwaki@geol.tsukuba.ac.jp
[†]These authors contributed equally to this work.

The 2022 submarine eruption of Hunga volcano, Tonga, was among the largest volcanic eruptions in the modern era, yet the processes controlling its explosive sequence remain poorly understood. Here we present the first detailed insight into the internal mechanics of an explosive cycle from teleseismic waveforms. Four eruptive episodes repeat an implosion-explosion cycle, separated by a 3-minute pause dominated by shear deformation. The cycles reveal an explosive engine driven by a hydraulically isolated, conduit-scale volume that is orders of magnitude smaller than the reservoir and re-pressurized between failures through seawater-driven phreatomagmatic inflow. Because recurrence is set by the repressurization rate of the sealed volume, the pace of an explosive sequence reflects the scale of its driving system, from minutes at conduit scale to days at reservoir scale.

The energetics of explosive volcanic eruptions are governed by accumulation of overpressure within a shallow magmatic system and pressure release through fragmentation (*1, 2*). The processes that control pressure cycles and failure within volcanic conduits are still poorly understood. For eruptions that consist of discrete episodes, resolving the complex history of pressure build-up and release is essential to identifying the mechanisms that sustain explosive output.

The 15 January 2022 submarine eruption of Hunga volcano, Tonga, was among the most energetic explosive events in the modern instrumental era (*3*). The eruption produced the tallest volcanic plume ever recorded, with height exceeding 58 km (*4, 5*), the largest stratospheric water injection of the satellite era (*6*), globe-encircling atmospheric Lamb waves (*7*), and the most intense lightning yet documented on Earth (*5*). The plume rose far higher than its modest tephra-fall deposit can account for, a discrepancy resolved by a column fed by ~90% steam by mass (*8*), identifying the submarine setting as a controlling factor. Post-eruption bathymetry shows a net loss of ~6 km^3 from within the ~2 km-radius caldera (*9*), above a multi-reservoir magmatic system imaged by marine gravity at 2–10 km depth (*10*) (Fig. 1). Seismic analyses resolved multiple discrete sub-events of moment magnitude 5–6 within the first 300 s, with a 160-s quiet period separating the first and the subsequent episodes (*3, 11, 12*).

The details of seafloor subsidence accompanying the 2022 eruption are poorly known. Surface deformation due to active calderas elsewhere is accommodated by slip on caldera-bounding faults, in modes ranging from piston-style uplift or subsidence through trapdoor faulting to progressive lateral failure (*13–16*), with recurrence between successive failures of hours to days. At Hunga, by contrast, successive sub-events recurred over seconds to minutes, and neither the mode of collapse nor its evolution through the sequence has been documented. Previous studies characterize each failure in isolation or restrict the polarity of the force (*17–20*), without addressing the system evolution between sub-events. The timing and history of individual failure episodes and the re-pressurization of the system between the failure episodes remain major unknowns.

Here we resolve the continuous volumetric changes of the shallow magmatic system during the Hunga eruptive phase and the associated momentum transfer to the solid Earth through the first 300 seconds. The resolved histories provide direct insights into the evolving internal mechanics of an explosive caldera collapse cycle. We show that the remarkable 2022 Hunga eruption was not a single event but a complex sequence in which a hydraulically isolated, conduit-scale volume re-pressurized through seawater-driven phreatomagmatic inflow and ruptured upon exceeding the strength of its confining seal. The short-duration cycle resolved at Hunga provides a new benchmark to which other explosive eruptions of different scales, settings, and styles can be compared.

Continuously imaging the Hunga eruption

We construct a composite source model of the Hunga eruption from teleseismic P waves recorded at 23 globally distributed stations (*21*) (Fig. 1; fig. S1). The composite model comprises a moment tensor with six independent components ($M_{rr}, M_{tt}, M_{pp}, M_{rt}, M_{rp}, M_{tp}$) and a centroid single force with three components (F_r, F_t, F_p), each represented as a continuous function of time (t). The moment tensor resolves the volumetric (M_{iso}) and shear deformation of the source region (*22, 23*); the single force resolves the momentum transfer between the source and the solid Earth (*24, 25*), with the vertical component F_r recording the net vertical exchange, including caldera subsidence. The source is fixed at 1 km depth beneath the caldera; as we show in Materials and Methods (*21*), the recovered source time history is largely insensitive to the assumed source depth.

The composite source model reveals four eruptive episodes separated by a 160-s apparent quiet period across the first 300 s of the eruption phase (Fig. 2; figs. S2, S3). Episode 1 occurred during the first 50 s, with the peak isotropic moment corresponding to a moment magnitude $M_W \sim 6.5$, and the peak vertical force of $F_r \sim 10^{14}$ N, among the largest reported for volcanic and mass-wasting sources (*24, 26*). Episode 1 began with an implosive onset (0–20 s), followed by the dominantly explosive phase (20–33 s), and ended with an implosive excursion (33–50 s), forming a complete implosion–explosion cycle (Fig. 2). This alternation is not a model artifact, because the unfiltered broadband P-wave displacement records exhibit coherent negative first motions across the network prior to the main explosion, confirming the implosive onset directly (Fig. 1; fig. S4). The F_r onset has a delay of 5–10 s relative to the M_{iso} onset (*21*) (fig. S5), suggesting that the source region began to deform as the seal gave way, before an open pathway to the surface was established. The multi-episode eruptive source history is consistent with the near-field tsunami record (*21*).

After 210 s, the eruption resumed, and Episodes 2 to 4 occurred in succession without intervening pauses, each lasting approximately 30 s and comprising a complete implosion–explosion cycle. The peak M_{iso} of Episode 2 is comparable to that of Episode 1, while Episodes 3 and 4 are progressively weaker. In contrast to Episode 1, M_{iso} and F_r resume simultaneously at the onset of Episodes 2 to 4 (*21*) (fig. S5), consistent with a pathway that already existed and had only to be reopened, rather than established.

The source mechanism during the four eruptive episodes is dominated by the isotropic moment, indicating that volumetric change of the shallow magmatic system, rather than shear failure, dominates the seismic radiation (Fig. 2). The centroid single forces are dominated by F_r throughout the episodes, with horizontal forces an order of magnitude smaller, consistent with the predominantly vertical momentum transfer to the solid Earth. Resolution tests confirm that the single force, the moment tensor, and its deviatoric part are each independently required; removing any of the parts increases the misfit significantly relative to the preferred model and exceeds the discrepancy threshold (fig. S3; Supplementary Texts S1, S2).

The temporal correlation between M_{iso} and F_r during the eruptive episodes follows from a shared driving mechanism. The isotropic moment scales with the reservoir overpressure ΔP (*27, 28*). The vertical single force has contributions from the momentum flux carried by discharged material and the static-pressure force coupling the source region to the solid Earth (*24, 25*). The momentum-flux contribution, the downward reaction to the upward discharge, is negligible, because even the upper bound on mass eruption rate ($\dot{m} \approx 5 \times 10^9$ kg/s from umbrella-cloud growth (*5*)) at Plinian velocities (e.g., 350 m/s (*8*)) yields $|\dot{m}v| \lesssim 1.8 \times 10^{12}$ N, less than 2% of the observed peak. The observed peak is instead upward and records the static-pressure coupling, the reaction to the downward redistribution of dense source-region material as the low-density fragmentation cavity expands and the overlying caldera roof subsides. The explosive volume increase ($M_{\mathrm{iso}} > 0$) and the downward mass redistribution ($F_r > 0$) are two expressions of the same depressurization-driven volatile exsolution and fragmentation (*1*), and M_{iso} and F_r vary in phase and with the same sign while the pathway connecting the source region to the surface is coherent.

The 160-s interval is the recharge phase of an explosive cycle

We argue that the 160-s interval between Episode 1 and Episode 2 is not a hiatus within the eruption. The volcano remained mechanically active, but the activity was redistributed across the source components. From 50 to 210 s, M_{iso} and F_r decayed to 16% and 22% of their Episode 1 root-mean-square amplitudes, while the off-diagonal moment-tensor component M_{rt} and the horizontal single force F_t retained 63% and 70% of their amplitudes. An envelope analysis (*21*) (fig. S7) shows that M_{rt} and F_t do not decay at all across the interval, whereas the volumetric and vertical-force components do. Passive viscoelastic relaxation in the source region cannot produce this pattern as it would decay every component on a common timescale set by the rheology of the surrounding viscoelastic halo (*29*). Synthetic recovery tests confirm that the persistent components are required by the data (*21*) (fig. S6), and P-wave back-projection images weak but coherent radiation throughout the interval (*12*). Shear deformation is therefore deduced to have continued while volumetric oscillation and vertical mass transfer were suppressed.

A partition of the total mechanical energy between shear and volumetric deformation is characterized by the deviatoric energy fraction f_{dev} (*21*) (Fig. 2). The latter holds at $f_{\mathrm{dev}} \approx 0.36$ through each eruptive episode, when volumetric change carries most of the energy, and increases to ≈ 0.7 during the 160-s interval, when shear dominates; the transition is robust to the choice of a smoothing window (*21*). The consistent value of $f_{\mathrm{dev}} \approx 0.36$ across the eruption episodes shows that the same explosive mechanism partitions energy during each episode. We note, however, that the teleseismic data cannot distinguish between a single conduit and several closely spaced ones.

The seismic observations are most simply explained by conduit sealing and recharge. When the conduit seals, the pathway connecting the source region to the surface closes, the static-pressure coupling that drives F_r vanishes, and the vertical mass flux ceases for the same reason. Without an open pathway the source region can no longer depressurize, so the volatile exsolution and fragmentation that drive the volumetric change cease, and M_{iso} decays accordingly. Shear deformation along the caldera-bounding structures, however, is mechanically separate from the conduit and continues independently of its state. Meanwhile magmatic and phreatomagmatic inflow rebuilds overpressure within the isolated shallow conduit volume, the Coulomb stress on the conduit walls increases and eventually enables slip as the system approaches the failure threshold (*29*). The implosive onset of Episode 2, like that of Episode 1, marks the moment the threshold is reached. The sealed volume contracts elastically as the seal fails, the conduit reopens, and coupled M_{iso}–F_r radiation resumes.

Alternative explanations may account for parts of the interval signature but not the whole sequence. A reduction in radiation efficiency would act on all source components alike and can neither produce the component-selective decay nor restore the coupled M_{iso}–F_r radiation at every subsequent onset. Sustained ring-fault slip without sealing (*30, 31*) would leave the static-pressure contribution to F_r unchanged, because an open conduit still transmits pressure forces, contrary to the observed decay of F_r throughout the interval. The vertical force itself has also drawn competing interpretations. Earlier single-force analyses obtained a net downward force (*18, 19, 32*), whereas our composite inversion yields a consistently upward force. Hu et al. (*20*) likewise obtained an upward F_r but attribute it to elastic rebound of the crust beneath a changing water column and interpret that the force records the changing surface load rather than an internal source process. The coupled M_{iso}–F_r behaviour during the episodes and the joint decay of both components into the interval are consistent with either interpretation. However, the persistent shear deformation during the interval is incompatible with the surface-load interpretation, which provides no mechanism for shear radiation during a pause in discharge. In contrast, conduit sealing requires it, because the accumulating overpressure brings the caldera-bounding faults closer to failure (Supplementary Text S3).

A time-compressed explosive engine

The peak vertical single force constrains the overpressure at failure. Because the momentum-flux contribution is less than 2% of the observed peak, the peak amplitude is dominated by the static-pressure coupling across the caldera roof, giving

$$\Delta P_{\mathrm{fail}} \approx \frac{|F_r|}{\pi r^2} \approx 8 \text{ MPa}, \tag{1}$$

where $r \approx 2{,}000$ m represents the radius of the caldera (*9*) and πr^2 is the area over which the overpressure couples to the solid Earth. A caldera-scale coupling area is required, since a conduit-scale coupling area would imply an overpressure of $\sim 10^3$ MPa or more, well above any plausible rock strength. The inferred excess pressure of 8 MPa falls within the tensile strength of andesitic volcanic rocks (7–11 MPa (*33*)), and it is also consistent with frictional strength of a conduit-scale plug overlying the sealed volume (*14, 34–36*). A force balance for plug ascent gives $\Delta P \approx \mu\, \Delta\rho\, g\, H^2/r_c$, where H and r_c are the plug height and radius, respectively, μ is the coefficient of friction, $\Delta\rho$ is the density difference between rock and water (assuming a hydrostatic pore pressure), and g is the gravitational acceleration (see (*21*)). It follows that a conduit-scale plug can sustain an overpressure of several megapascals for reasonable values of the in situ coefficient of friction (*15, 37, 38*), with a representative case yielding $\Delta P \approx 7$ MPa (*21*) (Fig. 3). Both failure modes thus predict an overpressure near the seismically inferred value, although the seismic observations alone do not distinguish between the failure modes.

If volume is injected into the sealed region at rate Q during the recharge interval, the overpressure reaches the failure threshold after

$$t_{\mathrm{fail}} = \frac{\Delta P_{\mathrm{fail}} \cdot V_{\mathrm{eff}}}{K \cdot Q}, \tag{2}$$

where V_{eff} is the effective volume of the sealed region and K is the bulk modulus of the contained fluid (*29*). Setting t_{fail} to the observed 160 s interval, with $\Delta P_{\mathrm{fail}} = 8$ MPa, $K = 0.5$ GPa appropriate for bubble-bearing magma (*23, 31*), requires $V_{\mathrm{eff}}/Q \approx 10^4$ s (Fig. 3).

For the climactic phase of the eruption, Q is the local rate at which magma and phreatomagmatic steam flow into the sealed region, not the long-term deep magmatic supply rate. The steam-dominated plume (*8*) records an intense magma–seawater interaction throughout the climactic phase, so the submarine setting can sustain a local inflow rate far above the deep magmatic supply. For Q between 10^3 and 10^4 m^3/s, V_{eff} falls between 10^7 and 10^8 m^3 (Fig. 3), two to three orders of magnitude smaller than the 27 km^3 shallow magmatic reservoir beneath the caldera inferred from gravity observations (*10*), but consistent with the volume of a shallow conduit having length comparable to the magma ascent path inferred from erupted ash (*39*). The 160-s cycle therefore engages the conduit and its immediately connected shallow volume rather than the entire caldera reservoir (Fig. 4). Because V_{eff} scales linearly with K, doubling K to 1.0 GPa doubles the inferred volume, which is still at least 100 times smaller than that of the reservoir.

Conduit-scale and reservoir-scale regimes of explosive caldera dynamics

The rapid cycle at Hunga, on the one hand, and the Kīlauea 2018 collapse sequence, on the other hand, occupy two physically distinct regimes of caldera failure dynamics. At Hunga, the 160-s recurrence timescale is shorter than the time required for pressure to diffuse across the deeper magmatic reservoir, so the climactic eruption operates at conduit scale. Conduit scale here refers to the compressible, hydraulically sealed volume that re-pressurizes between failures and thereby sets the recurrence interval. The erupted and collapsed material is supplied from the deeper reservoir through this volume, so the small V_{eff} gates the timing of the cycle rather than accommodating its mass budget. At Kīlauea, the day-long recurrence allows pressure to equilibrate across the reservoir, and the same scaling returns $V_{\mathrm{eff}} \approx 1$–$4$ km^3 (Fig. 3), consistent with the independently constrained reservoir volume of 1.1–9.7 km^3 (*15*). Obtaining the reservoir volume from the Kīlauea timescale supports the V_{eff}/Q scaling and the regime distinction. The same balance accommodates pressure changes of opposite sign, inflow-driven at Hunga and drainage-driven at Kīlauea. On a longer time scale, the 2018 Sierra Negra eruption, Galápagos, illustrates that a reservoir-scale cycle can also be driven by slow magmatic inflow at decadal recurrence (*40*).

The conduit-scale regime is not unique to Hunga. Crozier et al. (*41*) inferred that the Kīlauea 2018 collapse events drove moderate-scale explosive plumes through a stomp-rocket mechanism, in which abrupt subsidence compressed a pre-existing gas pocket of $\lesssim 10^6$ m^3 at the top of the reservoir. The reservoir therefore set the recurrence at Kīlauea while a far smaller volume generated each plume, so both scales operated within one sequence. The 2006 Augustine eruption shows a third mechanism, with explosive activity at hourly to daily intervals (*42*) attributed to bubble growth and pressure recovery within a confined shallow magmatic system above the deeper reservoir (*43*). The three cases differ in the energy that drives each cycle, from gravitational potential of the collapsing roof at Kīlauea, to magmatic gas at Augustine, to phreatomagmatic inflow at Hunga that refills the volume that the previous episode created. They share a regime in which a localized sub-reservoir volume rebuilds toward a failure threshold and discharges, with the recurrence set by the participating volume and the energy delivery rate. Textural evidence for the plug fracturing and resealing that resets such cycles has been documented at andesitic subaerial volcanoes (*36*).

At Pinatubo, Philippines, the 1991 cycle ran slowly enough to be read from the deposits and the eruption times. Thirteen explosions on 14–15 June preceded the climactic Plinian phase, at repose intervals that shortened until the supply rate could sustain continuous discharge. On 15 June, the climactic phase collapsed the summit into a 2.5-km caldera, after which sealing of small volumes restored discrete explosions at intervals that lengthened from 7 to 10 h as the pressurization rate decayed (*44*). Hoblitt et al. (*45*) inferred that magma entering the conduit during each repose dilated it elastically and that the conduit contracted during each explosion. The Hunga source-time history resolves an analogous cycle directly, driven by seawater-derived phreatomagmatic inflow rather than magmatic gas.

The submarine andesitic setting at Hunga favors the inflow-driven mechanism. Direct seawater access generates the phreatomagmatic steam that augments the inflow rate, and the shallow reservoir geometry (*10*) keeps the sealed volume small. Submarine arc volcanoes share these features broadly. The distinction between a single climactic explosion and a sustained inflow-driven cycle determines the hazard trajectory, since the atmospheric and tsunami hazards either remain confined to one event or escalate through the eruption, and continuous source reconstruction of future submarine eruptions can measure the sealed volume that separates the two outcomes.

Volcanic explosive engines have historically been characterized through their outputs, including pyroclastic deposits, atmospheric plumes, and climatic effects, with internal dynamics inferred from those outputs. At Hunga, the cycle was fast enough for the operating mechanics to be observed directly, and a regime distinction that had been physically argued became empirically testable. Submarine volcanism produces the majority of Earth's magmatic output and dominates the explosive record at oceanic arc and back-arc settings (*46*), yet sparse seafloor monitoring has left it characterized largely through its surface expression rather than through its operating physics. Comparable resolution at faster-cycling subaerial systems would test the regime classification across magma compositions, eruptive styles, and tectonic environments. Explosive volcanism remains among the most consequential and least directly observed processes in Earth's near-surface system. The continuous composite source reconstruction at Hunga is a step toward observing the system in operation.

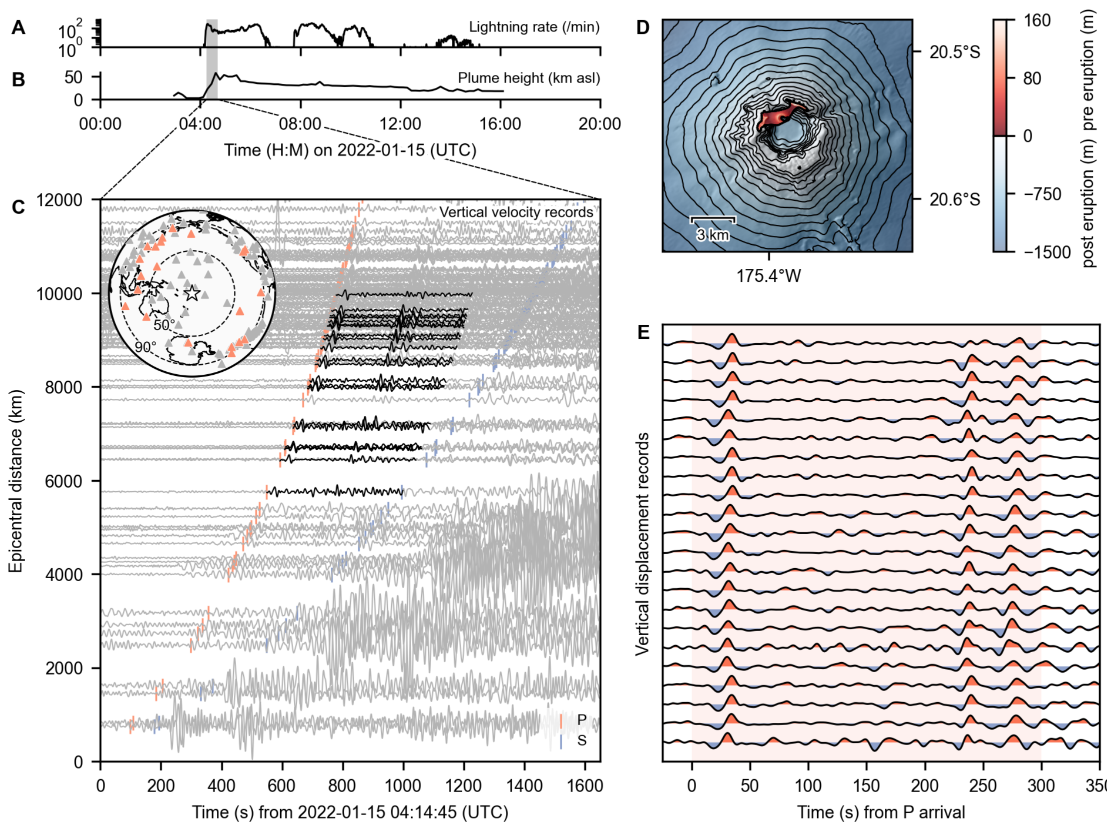

Figure 1: Summary of the study region and data. (A) Time series of lightning rate (within 20 km of the volcano) and (B) plume height (*5*). The gray shaded interval indicates the time window of panel (C). (C) Self-normalized, bandpass-filtered (10–70 s) vertical-component velocity records observed at the stations shown in the upper-left inset. Black traces are the records used for the source inversion. Red and blue markers denote the predicted P- and S-wave arrivals, respectively (*47*). The upper-left inset shows the station distribution and the Hunga volcano with the colored triangles denoting the stations and the star as the epicenter. Dashed circles denote epicentral distances. (D) Pre-eruption topography (September 2017) (*48*) and post-eruption bathymetry (*10*), with contours at 100 m intervals. (E) Self-normalized, bandpass-filtered (10–70 s) vertical-component displacement records at the stations shown as red triangles in the inset of panel (C). The time axis is referenced to the predicted P-wave arrival. The traces are sorted by epicentral distance, with positive and negative amplitudes filled in red and blue, respectively. Background shading marks the active-groups window analyzed in this study.

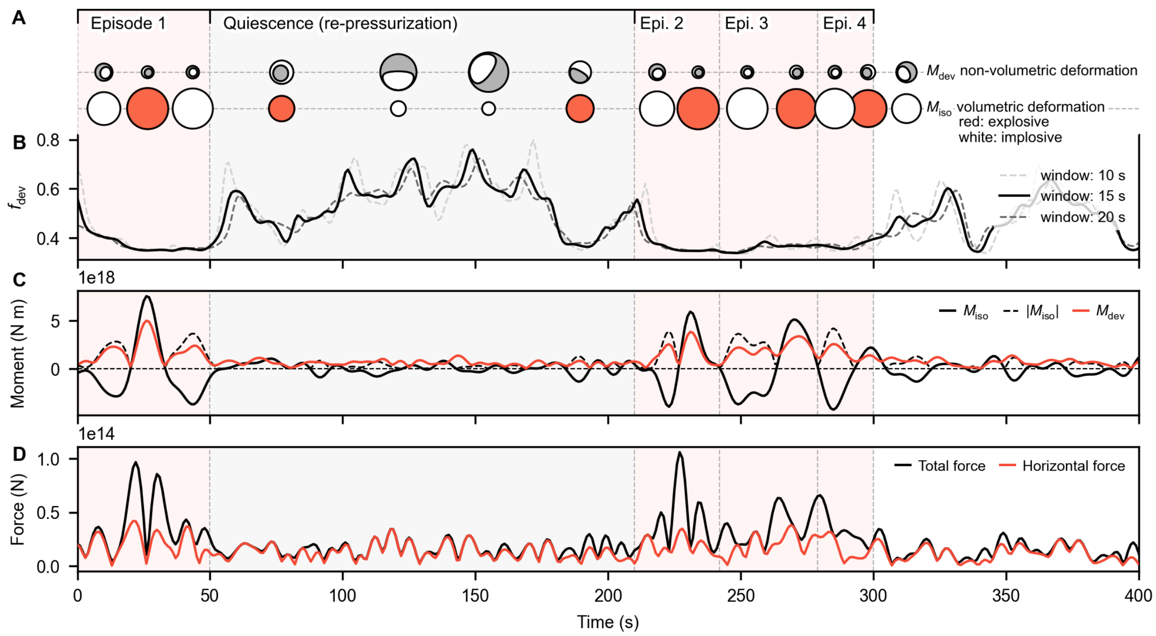

Figure 2: Time series of the source mechanism. Background shading indicates the intervals identified in the source time functions: Episode 1 eruption (0–50 s), the quiescence interval interpreted as conduit-scale re-pressurization (50–210 s), and Episodes 2–4 eruption (210–300 s). (A) Lower-hemisphere projections of the isotropic (M_{iso}, lower row) and deviatoric (M_{dev}, upper row) moment tensors, obtained by summing the corresponding moment tensors within consecutive sub-windows defined by zero crossings of M_{iso} (identified from sign changes, retaining only crossings separated by more than 10 samples to avoid spurious detections). Red and white circles denote explosive and implosive M_{iso}, respectively. The relative size of the M_{iso} and M_{dev} beachballs is scaled by the corresponding f_{dev}. (B) Deviatoric energy fraction $f_{\text{dev}}(t)$, computed with three smoothing window lengths (10, 15, 20 s). (C) Isotropic moment $M_{\text{iso}}(t)$ (solid black), its absolute value $|M_{\text{iso}}|(t)$ (dashed black), and the deviatoric moment $M_{\text{dev}}(t)$ (red). (D) Total centroid single force (black) and its horizontal component (red).

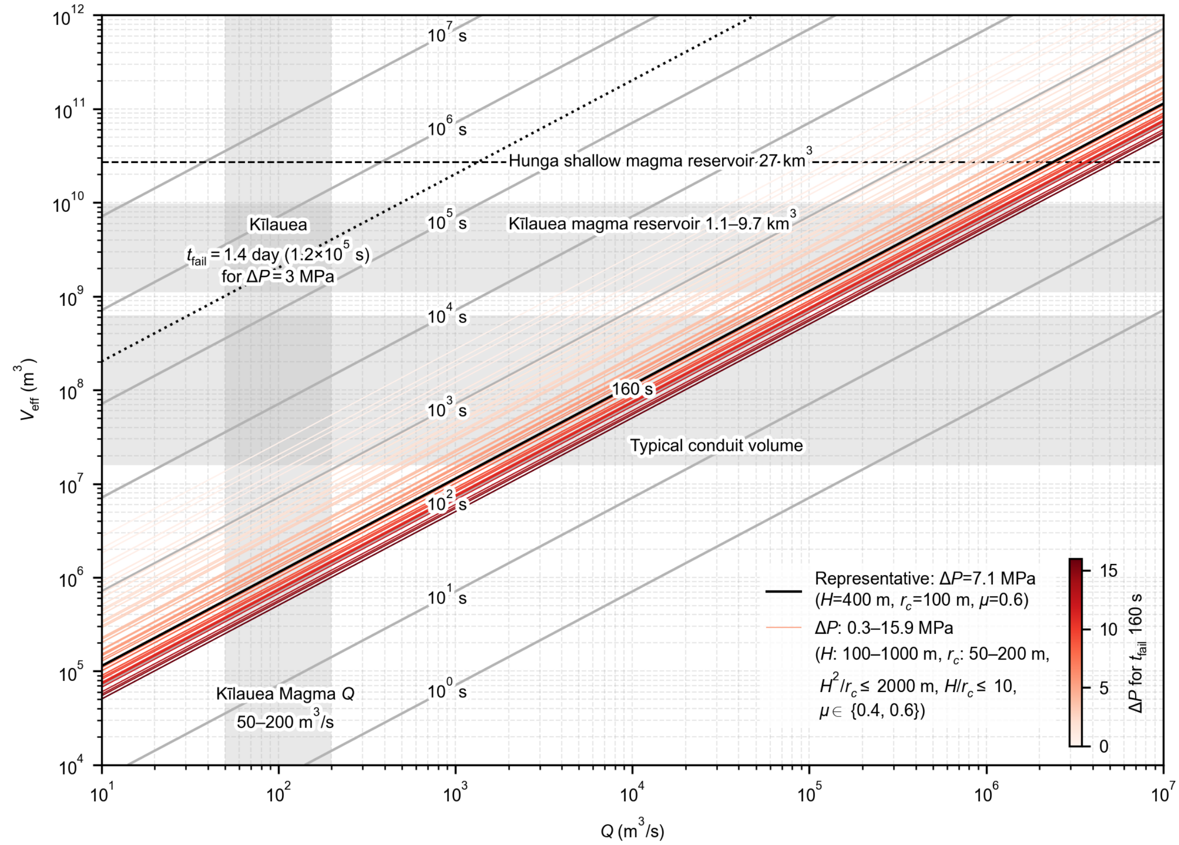

Figure 3: Scaling of t_{fail} for sealed-volume pressurization. Gray contours show $t_{\text{fail}} = \Delta P \cdot V_{\text{eff}}/(K \cdot Q)$ for the Hunga representative parameters ($\Delta P = 7.1$ MPa) (*21*), with contour values labeled in seconds. The black solid line marks the corresponding $t_{\text{fail}} = 160$ s contour. Red-shaded contours show the $t_{\text{fail}} = 160$ s loci for the full plausible range of plug parameters (*21*), with ΔP indicated by the colorbar. The dotted line shows the Kīlauea 2018 contour ($t_{\text{fail}} = 1.4$ day, $\Delta P = 3$ MPa, $K = 0.5$ GPa). Vertical shaded bands show volume flux ranges for Kīlauea magmatic effusion (*49*). The horizontal shaded band shows the Kīlauea reservoir volume (*15*); its intersection with the Kīlauea Q range and the dotted contour shows the scaling at a system whose recurrence timescale differs by three orders of magnitude. The dashed line marks the Hunga shallow magma reservoir (*10*); its intersection with the Hunga contour at the upper Q range would require reservoir-scale sealing and rupture every 160 s, inconsistent with the localized shear observed during the quiet period. The physically plausible Hunga regime lies within the conduit volume band, computed for a cylindrical conduit of radius $r_c = 50$–200 m and length 2000–5000 m (*50, 51*), with the conduit length comparable to the ascent path inferred for Hunga ash particles (*39*). The sealed volume in which overpressure accumulates and the caldera-scale area through which it couples to the solid Earth in Eq. (1) are distinct geometries of the same system.

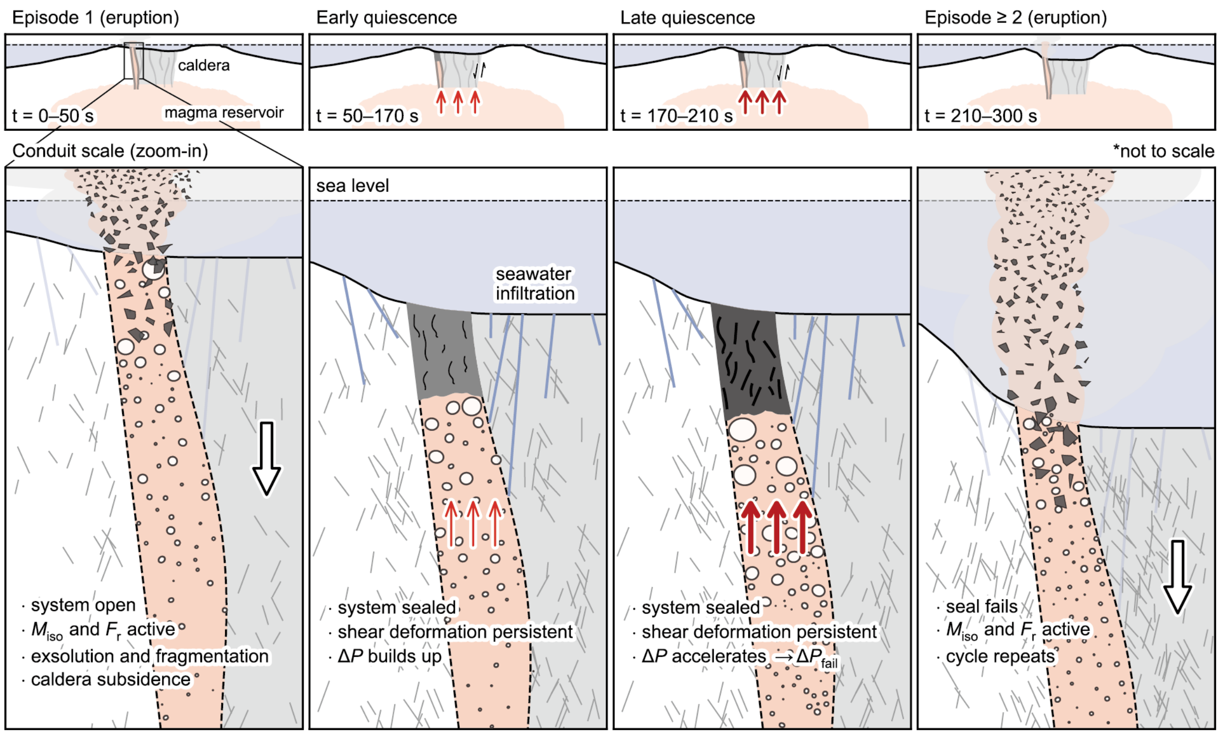

Figure 4: Schematic cross-section of the caldera-collapse cycle at Hunga. Top row, regional context; bottom row, conduit-scale zoom-in of the boxed region in the Episode 1 panel. The four columns show the mechanical progression inferred from the source time functions: Episode 1 eruption, with an open system, active M_{iso} and F_r, volatile exsolution and fragmentation, and caldera subsidence; early quiescence, with a sealed conduit, persistent shear deformation, and overpressure buildup; late quiescence, with continued sealing and overpressure approaching the failure threshold; and Episode ≥2, with seal failure and repetition of the cycle. Reddish shading denotes magma, and the dark cap denotes the sealed plug. Outlined arrows denote caldera-block subsidence; red arrows denote the overpressure buildup; blue lines denote seawater infiltration; and black single-headed arrows denote shear deformation along caldera-bounding structure. The panels are not to scale.

References and Notes

1. K. V. Cashman, R. S. J. Sparks, How volcanoes work: A 25 year perspective. *Geological Society of America Bulletin* **125** (5-6), 664–690 (2013), doi:10.1130/B30720.1, https://pubs.geoscienceworld.org/gsabulletin/article/125/5-6/664-690/125884.

2. K. H. Wohletz, Explosive magma-water interactions: Thermodynamics, explosion mechanisms, and field studies. *Bulletin of Volcanology* **48** (5), 245–264 (1986), doi:10.1007/BF01081754, http://link.springer.com/10.1007/BF01081754.

3. R. S. Matoza, *et al.*, Atmospheric waves and global seismoacoustic observations of the January 2022 Hunga eruption, Tonga. *Science (80-.).* **377** (6601), 95–100 (2022), doi:10.1126/science.abo7063, https://www.science.org/doi/epdf/10.1126/science.abo7063https://www.science.org/doi/10.1126/science.abo7063.

4. S. R. Proud, A. T. Prata, S. Schmauß, The January 2022 eruption of Hunga Tonga-Hunga Ha'apai volcano reached the mesosphere. *Science* **378** (6619), 554–557 (2022), doi:10.1126/science.abo4076, https://www.science.org/doi/10.1126/science.abo4076.

5. A. R. Van Eaton, *et al.*, Lightning Rings and Gravity Waves: Insights Into the Giant Eruption Plume From Tonga's Hunga Volcano on 15 January 2022. *Geophysical Research Letters* **50** (12), e2022GL102341 (2023), doi:10.1029/2022GL102341, https://agupubs.onlinelibrary.wiley.com/doi/10.1029/2022GL102341.

6. L. Millán, *et al.*, The Hunga Tonga-Hunga Ha'apai Hydration of the Stratosphere. *Geophysical Research Letters* **49** (13), e2022GL099381 (2022), doi:10.1029/2022GL099381, https://agupubs.onlinelibrary.wiley.com/doi/10.1029/2022GL099381.

7. P. Lynett, *et al.*, Diverse tsunamigenesis triggered by the Hunga Tonga-Hunga Ha'apai eruption. *Nature* **609** (7928), 728–733 (2022), doi:10.1038/s41586-022-05170-6, https://www.nature.com/articles/s41586-022-05170-6.

8. L. G. Mastin, A. R. Van Eaton, S. J. Cronin, Did steam boost the height and growth rate of the giant Hunga eruption plume? *Bull Volcanol* **86** (7), 64 (2024), doi:10.1007/s00445-024-01749-1, https://link.springer.com/10.1007/s00445-024-01749-1.

9. S. Seabrook, *et al.*, Volcaniclastic density currents explain widespread and diverse seafloor impacts of the 2022 Hunga Volcano eruption. *Nat Commun* **14** (1), 7881 (2023), doi:10.1038/s41467-023-43607-2, https://www.nature.com/articles/s41467-023-43607-2.

10. H. Le Mével, C. A. Miller, M. Ribó, S. Cronin, T. Kula, The magmatic system under Hunga volcano before and after the 15 January 2022 eruption. *Sci. Adv.* **9** (50), eadh3156 (2023), doi:10.1126/sciadv.adh3156, https://www.science.org/doi/10.1126/sciadv.adh3156.

11. Y. Zheng, *et al.*, Episodic Magma Hammers for the 15 January 2022 Cataclysmic Eruption of Hunga Tonga-Hunga Ha'apai. *Geophysical Research Letters* **50** (8), e2023GL102763 (2023), doi:10.1029/2023GL102763, https://agupubs.onlinelibrary.wiley.com/doi/10.1029/2023GL102763.

12. K. Tarumi, K. Yoshizawa, Eruption sequence of the 2022 Hunga Tonga-Hunga Ha'apai explosion from back-projection of teleseismic P waves. *Earth and Planetary Science Letters* **602**, 117966 (2023), doi:10.1016/j.epsl.2022.117966, `https://linkinghub.elsevier.com/retrieve/pii/S0012821X22006021`.

13. F. Amelung, S. Jónsson, H. Zebker, P. Segall, Widespread uplift and 'trapdoor' faulting on Galápagos volcanoes observed with radar interferometry. *Nature* **407** (6807), 993–996 (2000), doi:10.1038/35039604, `https://www.nature.com/articles/35039604`.

14. Y. Fialko, On origin of near-axis volcanism and faulting at fast spreading mid-ocean ridges. *Earth and Planetary Science Letters* **190** (1-2), 31–39 (2001), doi:10.1016/S0012-821X(01)00376-4, `https://linkinghub.elsevier.com/retrieve/pii/S0012821X01003764`.

15. P. Segall, K. Anderson, Repeating caldera collapse events constrain fault friction at the kilometer scale. *Proc. Natl. Acad. Sci. U.S.A.* **118** (30), e2101469118 (2021), doi:10.1073/pnas.2101469118, `https://pnas.org/doi/full/10.1073/pnas.2101469118`.

16. N. Geshi, I. Miyagi, G. Saito, C. E. Conway, Caldera collapse thresholds correlate with magma chamber dimensions. *Scientific Reports* **13** (1), 7463 (2023), doi:10.1038/s41598-023-34411-5, `https://www.nature.com/articles/s41598-023-34411-5`.

17. J. Thurin, C. Tape, R. Modrak, Multi-Event Explosive Seismic Source for the 2022 Mw 6.3 Hunga Tonga Submarine Volcanic Eruption. *The Seismic Record* **2** (4), 217–226 (2022), doi:10.1785/0320220027, `https://pubs.geoscienceworld.org/tsr/article/2/4/217/618354/Multi-Event-Explosive-Seismic-Source-for-the-2022`.

18. J. Thurin, C. Tape, Comparison of force and moment tensor estimations of subevents during the 2022 Hunga–Tonga submarine volcanic eruption. *Geophysical Journal International* **235** (2), 1959–1981 (2023), doi:10.1093/gji/ggad323, `https://academic.oup.com/gji/article/235/2/1959/7246059`.

19. R. Garza-Girón, T. Lay, F. Pollitz, H. Kanamori, L. Rivera, Solid Earth–atmosphere interaction forces during the 15 January 2022 Tonga eruption. *Sci. Adv.* **9** (2), eadd4931 (2023), doi:10.1126/sciadv.add4931, `https://www.science.org/doi/10.1126/sciadv.add4931`.

20. J. Hu, T. Phm, H. Tkalčić, A Composite Seismic Source Model for the First Major Event During the 2022 Hunga (Tonga) Volcanic Eruption. *Geophysical Research Letters* **51** (18), e2024GL109442 (2024), doi:10.1029/2024GL109442, `https://agupubs.onlinelibrary.wiley.com/doi/10.1029/2024GL109442`.

21. Materials and methods are available as supplementary material.

22. K. Aki, P. G. Richards, *Quantitative seismology* (University Science Books, Mill Valley, California New York), 2. edition, corrected printing ed. (2009).

23. T. Nishimura, Source mechanisms of volcanic explosion earthquakes: single force and implosive sources. *Journal of Volcanology and Geothermal Research* **86** (1-4), 97–106 (1998), doi:10.1016/S0377-0273(98)00088-2, `https://linkinghub.elsevier.com/retrieve/pii/S0377027398000882`.

24. H. Kanamori, J. W. Given, T. Lay, Analysis of seismic body waves excited by the Mount St. Helens eruption of May 18, 1980. *J. Geophys. Res.* **89** (B3), 1856–1866 (1984), doi:10.1029/JB089iB03p01856, https://agupubs.onlinelibrary.wiley.com/doi/10.1029/JB089iB03p01856.

25. K. R. Coppess, E. M. Dunham, M. Almquist, Ultra and Very Long Period Seismic Signatures of Unsteady Eruptions Predicted From Conduit Flow Models. *JGR Solid Earth* **127** (6), e2022JB024313 (2022), doi:10.1029/2022JB024313, https://agupubs.onlinelibrary.wiley.com/doi/10.1029/2022JB024313.

26. G. Ekström, C. P. Stark, Simple Scaling of Catastrophic Landslide Dynamics. *Science* **339** (6126), 1416–1419 (2013), doi:10.1126/science.1232887, https://www.science.org/doi/10.1126/science.1232887.

27. K. Mogi, Relations between the eruptions of various volcanoes and the deformations of the ground surfaces around them. *Bulletin of the Earthquake Research Institute* **36**, 99–134 (1958), doi:10.15083/0000033924, https://doi.org/10.15083/0000033924.

28. D. F. McTigue, Elastic stress and deformation near a finite spherical magma body: Resolution of the point source paradox. *Journal of Geophysical Research: Solid Earth* **92** (B12), 12931–12940 (1987), doi:10.1029/JB092iB12p12931, https://doi.org/10.1029/JB092iB12p12931.

29. P. Segall, *Earthquake and volcano deformation* (Princeton University Press, Princeton, N.J) (2010), https://press.princeton.edu/books/hardcover/9780691133027/earthquake-and-volcano-deformation.

30. A. Shuler, G. Ekström, M. Nettles, Physical mechanisms for vertical-CLVD earthquakes at active volcanoes. *JGR Solid Earth* **118** (4), 1569–1586 (2013), doi:10.1002/jgrb.50131, https://agupubs.onlinelibrary.wiley.com/doi/10.1002/jgrb.50131.

31. H. Kumagai, *et al.*, Very-Long-Period Seismic Signals and Caldera Formation at Miyake Island, Japan. *Science* **293** (5530), 687–690 (2001), doi:10.1126/science.1062136, https://www.science.org/doi/10.1126/science.1062136.

32. F. F. Pollitz, R. Garza-Giron, T. Lay, Comment on "Multievent Explosive Seismic Source for the 2022 Mw 6.3 Hunga Tonga Submarine Volcanic Eruption" by Julien Thurin, Carl Tape, and Ryan Modrak. *The Seismic Record* **3** (3), 210–214 (2023), doi:10.1785/0320230003, https://pubs.geoscienceworld.org/tsr/article/3/3/210/627527/Comment-on-Multievent-Explosive-Seismic-Source-for.

33. P. M. Benson, *et al.*, Laboratory simulations of tensile fracture development in a volcanic conduit via cyclic magma pressurisation. *Earth and Planetary Science Letters* **349-350**, 231–239 (2012), doi:10.1016/j.epsl.2012.07.003, https://linkinghub.elsevier.com/retrieve/pii/S0012821X12003627.

34. R. M. Iverson, *et al.*, Dynamics of seismogenic volcanic extrusion at Mount St Helens in 2004–05. *Nature* **444** (7118), 439–443 (2006), doi:10.1038/nature05322, https://www.nature.com/articles/nature05322.

35. J. Johnson, J. Lees, Plugs and chugs—seismic and acoustic observations of degassing explosions at Karymsky, Russia and Sangay, Ecuador. *Journal of Volcanology and Geothermal Research* **101** (1-2), 67–82 (2000), doi:10.1016/S0377-0273(00)00164-5, `https://linkinghub.elsevier.com/retrieve/pii/S0377027300001645`.

36. K. Matsumoto, N. Geshi, Repeated fracturing-healing behavior of lava plugs drives intermittent explosions during Vulcanian eruptions. *Geology* **54** (7), 647–651 (2026), doi:10.1130/G54286.1, `https://pubs.geoscienceworld.org/geology/article/54/7/647/728335/Repeated-fracturing-healing-behavior-of-lava-plugs`.

37. J. Byerlee, Friction of rocks. *pure and applied geophysics* **116** (4), 615–626 (1978), doi:10.1007/BF00876528, `https://doi.org/10.1007/BF00876528`.

38. Y. Fialko, Estimation of Absolute Stress in the Hypocentral Region of the 2019 Ridgecrest, California, Earthquakes. *Journal of Geophysical Research: Solid Earth* **126** (7), e2021JB022000 (2021), doi:10.1029/2021JB022000, `https://agupubs.onlinelibrary.wiley.com/doi/10.1029/2021JB022000`.

39. J. Wu, *et al.*, Low sulfur emissions from 2022 Hunga eruption due to seawater–magma interactions. *Nat. Geosci.* **18** (6), 518–524 (2025), doi:10.1038/s41561-025-01691-7, `https://www.nature.com/articles/s41561-025-01691-7`.

40. P. M. Gregg, *et al.*, Forecasting mechanical failure and the 26 June 2018 eruption of Sierra Negra Volcano, Galápagos, Ecuador. *Sci. Adv.* **8** (22), eabm4261 (2022), doi:10.1126/sciadv.abm4261, `https://www.science.org/doi/10.1126/sciadv.abm4261`.

41. J. Crozier, *et al.*, Explosive 2018 eruptions at Kīlauea driven by a collapse-induced stomp-rocket mechanism. *Nat. Geosci.* **17** (6), 572–578 (2024), doi:10.1038/s41561-024-01442-0, `https://www.nature.com/articles/s41561-024-01442-0`.

42. J. Power, D. Lalla, Seismic observations of Augustine Volcano, 1970-2007 (17691), 3–40 (2010), doi:10.3133/pp17691, `https://pubs.usgs.gov/publication/pp17691`.

43. P. B. Dawson, B. A. Chouet, J. Power, Determining the seismic source mechanism and location for an explosive eruption with limited observational data: Augustine Volcano, Alaska: ERUPTION MECHANISM AT AUGUSTINE. *Geophys. Res. Lett.* **38** (3), n/a–n/a (2011), doi:10.1029/2010GL045977, `http://doi.wiley.com/10.1029/2010GL045977`.

44. E. W. Wolfe, R. P. Hoblitt, Overview of the Eruptions, in *Fire and Mud: Eruptions and Lahars of Mount Pinatubo, Philippines*, C. G. Newhall, R. S. Punongbayan, Eds. (University of Washington Press, Seattle) (1996), `https://pubs.usgs.gov/pinatubo/wolfe/`.

45. R. P. Hoblitt, *et al.*, The Preclimactic Eruptions of Mount Pinatubo, June 1991, in *Fire and Mud: Eruptions and Lahars of Mount Pinatubo, Philippines*, C. G. Newhall, R. S. Punongbayan, Eds. (University of Washington Press, Seattle), pp. 457–511 (1996), `https://pubs.usgs.gov/pinatubo/hoblitt2/`.

46. I. C. Wright, *et al.*, Collapse and reconstruction of Monowai submarine volcano, Kermadec arc, 1998–2004. *Journal of Geophysical Research: Solid Earth* **113** (B8), 2007JB005138

(2008), doi:10.1029/2007JB005138, https://agupubs.onlinelibrary.wiley.com/doi/10.1029/2007JB005138.

47. A. M. Dziewonski, D. L. Anderson, Preliminary reference Earth model. *Phys. Earth Planet. Inter.* **25** (4), 297–356 (1981), doi:10.1016/0031-9201(81)90046-7, http://www.sciencedirect.com/science/article/pii/0031920181900467https://linkinghub.elsevier.com/retrieve/pii/0031920181900467.

48. J. B. Garvin, *et al.*, Monitoring and Modeling the Rapid Evolution of Earth's Newest Volcanic Island: *Hunga Tonga Hunga Ha'apai* (Tonga) Using High Spatial Resolution Satellite Observations. *Geophysical Research Letters* **45** (8), 3445–3452 (2018), doi:10.1002/2017GL076621, https://agupubs.onlinelibrary.wiley.com/doi/10.1002/2017GL076621.

49. C. A. Neal, *et al.*, The 2018 rift eruption and summit collapse of Kīlauea Volcano. *Science* **363** (6425), 367–374 (2019), doi:10.1126/science.aav7046, https://www.science.org/doi/10.1126/science.aav7046.

50. R. Scandone, S. D. Malone, Magma supply, magma discharge and readjustment of the feeding system of mount St. Helens during 1980. *Journal of Volcanology and Geothermal Research* **23** (3-4), 239–262 (1985), doi:10.1016/0377-0273(85)90036-8, https://linkinghub.elsevier.com/retrieve/pii/0377027385900368.

51. A. Costa, R. Sparks, G. Macedonio, O. Melnik, Effects of wall-rock elasticity on magma flow in dykes during explosive eruptions. *Earth and Planetary Science Letters* **288** (3-4), 455–462 (2009), doi:10.1016/j.epsl.2009.10.006, https://linkinghub.elsevier.com/retrieve/pii/S0012821X09006050.

52. Geoscience Australia, Australian National Seismograph Network Data Collection (2021), doi:10.26186/144675, http://pid.geoscience.gov.au/dataset/ga/144675.

53. Universidad de Chile, Red Sismologica Nacional (2012), doi:10.7914/SN/C1, https://www.fdsn.org/networks/detail/C1/.

54. California Institute of Technology and United States Geological Survey Pasadena, Southern California Seismic Network (1926), doi:10.7914/SN/CI, https://www.fdsn.org/networks/detail/CI/.

55. Albuquerque Seismological Laboratory (ASL)/USGS, Caribbean Network (2006), doi:10.7914/SN/CU, https://www.fdsn.org/networks/detail/CU/.

56. Albuquerque Seismological Laboratory (ASL)/USGS, Global Telemetered Seismograph Network (USAF/USGS) (1993), doi:10.7914/SN/GT, https://www.fdsn.org/networks/detail/GT/.

57. Hong Kong Observatory, Hong Kong Seismograph Network (2009), http://www.hko.gov.hk/gts/equake/sp_seismo_network_intro_e.htm.

58. Albuquerque Seismological Laboratory (ASL)/USGS, New China Digital Seismograph Network (1992), doi:10.7914/SN/IC, https://www.fdsn.org/networks/detail/IC/.

59. EarthScope Consortium, Global Seismograph Network - II (1986), doi:10.7914/SN/II, https://www.fdsn.org/networks/detail/II/.

60. Various Institutions, International Miscellaneous Stations (1965), doi:10.7914/VEFQ-VH75, https://www.fdsn.org/networks/detail/IM/.

61. Albuquerque Seismological Laboratory/USGS, Global Seismograph Network (GSN - IRIS/USGS) (1988), doi:10.7914/SN/IU, https://www.fdsn.org/networks/detail/IU/.

62. Flanders Marine Institute (VLIZ); Intergovernmental Oceanographic Commission (IOC), Sea level station monitoring facility (2021), doi:10.14284/482, https://doi.org/10.14284/482.

63. R. Okuwaki, W. Fan, O. Sandanbata, D. C. Roman, Y. Fialko, Code and data for source inversion of the 2022 Hunga submarine eruption (2026), doi:10.5281/zenodo.21397417, https://doi.org/10.5281/zenodo.21397417.

64. U.S. Geological Survey Earthquake Hazards Program, Advanced National Seismic System (ANSS) Comprehensive Catalog of Earthquake Events and Products (2017), doi:10.5066/F7MS3QZH, https://doi.org/10.5066/F7MS3QZH.

65. W. Fan, P. M. Shearer, P. Gerstoft, Kinematic earthquake rupture inversion in the frequency domain. *Geophysical Journal International* **199** (2), 1138–1160 (2014), doi:10.1093/gji/ggu319, http://academic.oup.com/gji/article/199/2/1138/625388/Kinematic-earthquake-rupture-inversion-in-the.

66. M. Van Driel, L. Krischer, S. C. Stähler, K. Hosseini, T. Nissen-Meyer, Instaseis: instant global seismograms based on a broadband waveform database. *Solid Earth* **6** (2), 701–717 (2015), doi:10.5194/se-6-701-2015, https://se.copernicus.org/articles/6/701/2015/.

67. X. Luo, W. Fan, Y. Fialko, A Joint Seismic and Space-Based Investigation of the 2016 Lamplugh Glacier and 2017 Wrangell Mountains (Alaska) Landslides. *JGR Earth Surface* **128** (3), e2022JF006903 (2023), doi:10.1029/2022JF006903, https://agupubs.onlinelibrary.wiley.com/doi/10.1029/2022JF006903.

68. M. Yuan, Y. Lin, Model selection and estimation in regression with grouped variables. *J. R. Stat. Soc. Ser. B (Statistical Methodol.* **68** (1), 49–67 (2006), doi:https://doi.org/10.1111/j.1467-9868.2005.00532.x, https://doi.org/10.1111/j.1467-9868.2005.00532.x.

69. A. Beck, M. Teboulle, A Fast Iterative Shrinkage-Thresholding Algorithm for Linear Inverse Problems. *SIAM J. Imaging Sci.* **2** (1), 183–202 (2009), doi:10.1137/080716542, https://epubs.siam.org/doi/10.1137/080716542.

70. H. W. Engl, M. Hanke, A. Neubauer, *Regularization of inverse problems*, vol. 375 (Springer Science & Business Media) (1996), https://link.springer.com/book/9780792341574.

71. P. C. Hansen, *Rank-Deficient and Discrete Ill-Posed Problems* (Society for Industrial and Applied Mathematics) (1998), doi:10.1137/1.9780898719697, https://epubs.siam.org/doi/abs/10.1137/1.9780898719697.

72. O. Sandanbata, *et al.*, Sub-Decadal Volcanic Tsunamis Due To Submarine Trapdoor Faulting at Sumisu Caldera in the Izu–Bonin Arc. *JGR Solid Earth* **127** (9), e2022JB024213 (2022), doi:10.1029/2022JB024213, https://agupubs.onlinelibrary.wiley.com/doi/10.1029/2022JB024213.

73. J. C. Borrero, D. Greer, H. Damlamian, Tsunami Hazard Assessment for Tongatapu, Tonga, in *Australasian Coasts & Ports 2021: Te Oranga Takutai, Adapt and Thrive*, pp. 141–147 (2021), https://search.informit.org/doi/10.3316/informit.245328978802903.

74. ITIC Tsunami Bulletin Board, [Tsunami_BB] Bathymetry Data for modelling the Tonga Tsunami, https://list.woc.noaa.gov/private/tsunami_bb/2022-February/000236.html (2022), retrieved 9 July 2026.

75. K. Mackay, Digital Elevation Models of Hunga Volcano: Pre- and Post- 15 January 2022 Eruption (2022), doi:10.5281/zenodo.7456324, https://doi.org/10.5281/zenodo.7456324.

76. GEBCO Bathymetric Compilation Group, The GEBCO_2026 Grid: a Continuous Terrain Model for Oceans and Land at 15 Arc-Second Intervals (2026), doi:10.5285/4f68d5c7-45eb-f999-e063-7086abc036fa, https://doi.org/10.5285/4f68d5c7-45eb-f999-e063-7086abc036fa.

77. Bureau of Meteorology, Metadata for Tidal Data Exchange: Nuku'alofa, Tonga, https://www.bom.gov.au/ntc/IDO50000/IDO50000_66600.pdf (2025), accessed 26 July 2026.

78. T. Baba, *et al.*, Parallel Implementation of Dispersive Tsunami Wave Modeling with a Nesting Algorithm for the 2011 Tohoku Tsunami. *Pure and Applied Geophysics* **172** (12), 3455–3472 (2015), doi:10.1007/s00024-015-1049-2, https://doi.org/10.1007/s00024-015-1049-2.

79. B. Le Méhauté, Theory of Explosion-Generated Water Waves, in *Advances in Hydroscience*, V. T. Chow, Ed. (Elsevier), vol. 7, pp. 1–79 (1971), doi:10.1016/B978-0-12-021807-3.50006-0, https://doi.org/10.1016/B978-0-12-021807-3.50006-0.

80. S. M. Day, K. L. McLaughlin, Seismic source representations for spall. *Bulletin of the Seismological Society of America* **81** (1), 191–201 (1991), doi:10.1785/BSSA0810010191, https://pubs.geoscienceworld.org/bssa/article/81/1/191/119441/Seismic-source-representations-for-spall.

81. P. Poli, N. M. Shapiro, Rapid Characterization of Large Volcanic Eruptions: Measuring the Impulse of the Hunga Tonga Ha'apai Explosion From Teleseismic Waves. *Geophysical Research Letters* **49** (8), e2022GL098123 (2022), doi:10.1029/2022GL098123, https://agupubs.onlinelibrary.wiley.com/doi/10.1029/2022GL098123.

82. Y. Zhu, *et al.*, Long-Period Seismic Waves From Seawater Disturbances During the 2018 Anak Krakatau Volcanic Island Collapse. *Geophysical Research Letters* **53** (5), e2025GL119807 (2026), doi:10.1029/2025GL119807, https://agupubs.onlinelibrary.wiley.com/doi/10.1029/2025GL119807.

Acknowledgments

Funding: RO was funded by JSPS Grant-in-Aid for Scientific Research (B) 24K00726. OS was funded by JSPS Grant-in-Aid for Early-Career Scientists 24K17141.

Author contributions: R.O. and W.F. equally contributed to the study. R.O. and W.F. conceived the study and led the research. R.O. and W.F. developed the inversion method and wrote the analysis code. R.O. performed the inversions and produced the figures. R.O. and W.F. wrote the initial draft of the manuscript. O.S. contributed to the tsunami calculation and the interpretation of the volcanic-source mechanism. D.C.R. contributed to the interpretation of the eruption dynamics and the physical mechanism of the explosive cycle. Y.F. developed the frictional force-balance and re-pressurization scaling framework. All authors contributed to interpreting the results and editing the manuscript.

Competing interests: There are no competing interests to declare.

Data, code and materials availability: The seismic waveform data and related metadata analyzed in this study are publicly available through the International Federation of Digital Seismograph Networks (FDSN) web service (`https://www.fdsn.org/webservices/`), using the networks AU (*52*), C1 (*53*), CI (*54*), CU (*55*), GT (*56*), HK (*57*), IC (*58*), II (*59*), IM (*60*), and IU (*61*). The tide-gauge record is available through the VLIZ-UNESCO/IOC sea level station monitoring facility (*62*). The code to reproduce the results of this study is deposited at Zenodo (`https://doi.org/10.5281/zenodo.21397417`) (*63*) and will be made publicly available upon publication.

Supplementary Materials

Materials and Methods

Composite source inversion

We use seismic data from the globally distributed broadband networks in the epicentral range 50°–90°. The data window begins at a theoretical P-wave arrival from the event origin time at 2022-01-15T04:14:45 (UTC) (*64*) predicted by the PREM model (*47*) and extends for a fixed 450 s from the P arrival. The epicentral range and the data window target teleseismic P-wave arrivals while avoiding the complexity and interference of other untargeted phases at shorter distances. The data are deconvolved to velocity after removing the instrumental responses and bandpass-filtered to 10–70 s period using a fourth-order zero-phase Butterworth filter. The frequency-domain inversion described below is performed within the same passband. Each available channel is screened by signal-to-noise ratio (SNR), defined as the ratio of the peak amplitude in the signal window to the root-mean-square amplitude of a noise window preceding the predicted P-wave arrival. Channels with SNR < 10 are discarded. After screening, 23 channels (22 vertical and 1 north–south component) were retained for the frequency-domain inversion (*65*).

For a point source, the seismic waveform at frequency ω can be written in vector-matrix notation as

$$\mathbf{d}(\omega) \;=\; \mathbf{G}(\omega)\,\mathbf{s}(\omega), \tag{S1}$$

where $\mathbf{d}(\omega)$ is the data vector across N_j channels, $\mathbf{G}(\omega)$ is the Green's function matrix, and $\mathbf{s}(\omega)$ is the source vector. The source vector comprises $N_m = 9$ components: the six independent moment tensor (MT) components M_{rr}, M_{tt}, M_{pp}, M_{rt}, M_{rp}, M_{tp} and the three single force (SF) components F_r, F_t, F_p, all in spherical coordinates (r, t, p). For each discrete frequency ω_k in the inversion band, the problem in Eq. (S1) is solved by ordinary least squares:

$$\hat{\mathbf{s}}(\omega_k) \;=\; \arg\min_{\mathbf{s}} \left\| \mathbf{G}(\omega_k)\,\mathbf{s} - \mathbf{d}(\omega_k) \right\|_2^2. \tag{S2}$$

No explicit regularization is applied to the frequency-domain inversion. The source time history for each component m is obtained by inverse fast Fourier transform: $s_m(t) = \mathcal{F}^{-1}\left[\hat{s}_m(\omega)\right]$, where $\hat{s}_m(\omega) = 0$ outside the inversion band. The resulting $s_m(t)$ is a bandlimited, causal source time function where $t = 0$ corresponds to the hypothesized event origin time. The quality of the waveform fit is evaluated by the normalized ℓ_1 misfit, defined as the ratio of the ℓ_1 norm of the residual to that of the observed waveform, summed across all channels:

$$\ell_1 = \frac{\sum_j |d_j(t) - \hat{d}_j(t)|}{\sum_j |d_j(t)|}, \tag{S3}$$

where $d_j(t)$ and $\hat{d}_j(t)$ are the observed and predicted amplitudes at channel j at time t. Green's functions were computed with Instaseis (*66*) using the `prem_a_5s` axisymmetric spectral-element database, which provides broadband, pre-computed responses for a spherically symmetric Earth model. The source was placed at 1 km depth, latitude 20.546°S, longitude 175.390°W (*64*). The shallow reference depth is supported by the 2–10 km magmatic reservoir inferred from marine gravity at Hunga (*10*). To verify that the recovered source process does not depend on this assumption, we repeated the nine-component inversion at 20 trial depths from 0.5 to 10 km at 0.5 km intervals, recomputing Green's functions for each depth and keeping all other parameters identical. The temporal source pattern discussed in the main text is stable across all tested depths, with the ℓ_1 misfit varying by less than 5%, comparable to the bootstrap variation reported below (±5%) and an order of magnitude smaller than the misfit penalties incurred by removing either the MT or the SF source type (see below). The weak depth dependence is consistent with the limited depth resolution of teleseismic inversions for this event (*18*). For each station, Instaseis returns nine elementary seismograms corresponding to the unit excitation of each source component. These were Fourier-transformed to yield the kernel matrix $\mathbf{G}(\omega)$.

After we obtain the solution, we assess its robustness through a bootstrap resampling test (*67*). Let Q denote the set of N_q qualified channels from the optimum run. For each of $N_B = 1000$ realizations, we draw a random subset of $\lfloor 0.8\, N_q \rfloor$ channels from Q without replacement and solve Eq. (S2) using only those channels, yielding a bootstrap source spectrum $\hat{\mathbf{s}}^{(b)}(\omega)$. All bootstrap spectra are then transformed to the time domain, $s_m^{(b)}(t) = \mathcal{F}^{-1}[\hat{s}_m^{(b)}(\omega)]$, and a 95% confidence interval is computed as $\mathrm{CI}_{95}[s_m(t)] = \bar{s}_m(t) \pm 1.96\,\sigma_m(t)$, where $\bar{s}_m$ and σ_m are the mean and standard deviation over the N_B realizations.

The predicted waveforms from the composite nine-component inversion reproduce the principal features of the observed records across all 23 channels, including the initial large-amplitude P-wave arrival, the lower-amplitude coda, and the renewed arrivals associated with the later eruptive episodes. The ℓ_1 misfit is $\ell_1 = 0.605$; bootstrap resampling yields $\ell_1 = 0.674 \pm 0.034$, confirming that the solution is not controlled by a small subset of stations. Separate inversions using only the six MT components or only the three SF components yield $\ell_1 = 0.791$ (+31%) and $\ell_1 = 0.921$ (+52%), respectively, demonstrating that each source type captures waveform features the other cannot reproduce (fig. S1). We conclude that a composite source model is required by the data.

To characterize how the source mechanism evolves across the eruptive sequence, we decompose the full moment tensor at each time sample into its isotropic and deviatoric parts and compute a time-varying deviatoric energy fraction. Denoting the isotropic moment as $M_{\mathrm{iso}}(t) = (M_{rr}(t) + M_{tt}(t) + M_{pp}(t))/3$ and the deviatoric moment tensor as $M_{ij}^{\mathrm{dev}}(t) = M_{ij}(t) - M_{\mathrm{iso}}(t)$, we define the Frobenius norms $E_{\mathrm{iso}}(t) = 3M_{\mathrm{iso}}^2(t)$ and $E_{\mathrm{dev}}(t) = \sum_i (M_{ii}^{\mathrm{dev}}(t))^2 + 2\sum_{i<j}(M_{ij}^{\mathrm{dev}}(t))^2$. Because the isotropic and deviatoric subspaces are orthogonal under the Frobenius inner product, the total energy partitions exactly: $\|M_{ij}\|_F^2 = E_{\mathrm{iso}} + E_{\mathrm{dev}}$, which enables the quantitative comparison between the two. The smoothed deviatoric fraction is then

$$f_{\mathrm{dev}}(t) = \frac{\langle E_{\mathrm{dev}} \rangle_T^{1/2}}{\langle E_{\mathrm{dev}} \rangle_T^{1/2} + \langle E_{\mathrm{iso}} \rangle_T^{1/2}}, \tag{S4}$$

where $\langle\cdot\rangle_T$ denotes a moving average with window length T. We computed $f_{\mathrm{dev}}(t)$ for $T \in \{10, 15, 20\}$ s and found the temporal pattern to be insensitive to this choice (Fig. 2).

Pre-event noise floor estimation

To establish a baseline noise floor for each of the nine source components, we repeated the frequency-domain inversion using a pre-P-wave noise window as input data while retaining the identical Green's function matrix used in the signal inversion. For each station, a 160 s window ending 30 min before the predicted P-wave arrival was extracted from the bandpass-filtered (10–70 s) velocity record. These noise segments were substituted into the data spectrum matrix, and the inversion was carried out with the same station set, frequency bins, and least-squares procedure as the signal analysis. The resulting nine-component source time functions represent the amplitude level that the inversion machinery produces when no coherent source signal is present. We define the noise floor $\sigma_m^{\mathrm{noise}}$ for each component m as the root-mean-square amplitude of the corresponding noise-derived source time function. The quiet-period RMS amplitudes of the inversion signal (computed over $t = 50$–210 s) exceed the corresponding noise floors by factors of 6–18 across all nine components, with the smallest margin for M_{rt} (factor of 6) and the largest for the diagonal moment-tensor components (factors of ~18). This confirms that the quiet-period source amplitudes are not artifacts of the inversion procedure (fig. S2).

Group-sparse post-processing

The frequency-domain inversion yields a source time history **s** that is non-zero at many time samples, some of which could be noise artifacts. It is possible that true volcanic activity occurs only in a few contiguous episodes rather than in many isolated samples. To test this, we apply a group-sparse post-processing step to evaluate the smallest number of active source episodes required to explain the observations within the known noise level. This step does not redefine the primary inversion but serves as an independent assessment of which source intervals are genuinely required by the data.

We partition the source time axis into non-overlapping contiguous windows of duration L seconds and solve the group lasso problem

$$\min_{\mathbf{s}} \ \tfrac{1}{2}\|\mathbf{W}(\mathbf{d}-\mathbf{G}\mathbf{s})\|_2^2 \ + \ \lambda \sum_{g\in\mathcal{G}} \|\mathbf{s}_g\|_2, \tag{S5}$$

where $\mathbf{W} = \mathrm{diag}(1/\sigma_1,\ldots,1/\sigma_{N_j})$ is a channel-wise whitening operator with per-channel noise standard deviations σ_j estimated from the post-signal portion of the observed waveform, and $\mathbf{s}_g$ is the subvector of source samples within group g (*68*). The post-signal estimate is deliberately conservative: residual coda energy may cause σ_j to be overestimated, raising the effective noise floor and making the χ^2 acceptance criterion harder to satisfy, so any source interval that survives this more stringent test is robustly required by the data. The penalty acts on the group norm rather than on individual samples, so a physically plausible episode containing, for example, both explosive and implosive phases is treated as a single active interval. Only windows with $t \geq 0$ are penalized; pre-event windows are retained freely to absorb pre-signal energy. Equation (S5) is solved over a path of λ values using Fast Iterative Shrinkage-Thresholding Algorithm (FISTA) (*69*), and at each λ the active groups (those with $\|\mathbf{s}_g\|_2 > 10^{-6}$) define a support Ω.

The sparsity penalty shrinks amplitudes. Once the support Ω has been identified, the source amplitudes are refitted without penalty:

$$\mathbf{s}_{\mathrm{refit}} \ = \ \arg \min_{\mathbf{s}:\,\mathrm{supp}(\mathbf{s})\subseteq\Omega} \|\mathbf{W}(\mathbf{d}-\mathbf{G}\mathbf{s})\|_2^2. \tag{S6}$$

In practice this is solved as a Tikhonov-stabilized least squares on the reduced kernel $\mathbf{G}^{\mathrm{red}}$ (columns of $\mathbf{G}$ corresponding to Ω), with regularization parameter $\alpha = 10^2$. The sparsest model whose refit misfit satisfies

$$\chi^2_{\mathrm{refit}} \ \leq \ 1.1\,\chi^2_{\mathrm{base}}, \tag{S7}$$

where $\chi^2_{\mathrm{base}} = \|\mathbf{W}(\mathbf{d}-\mathbf{G}\mathbf{s}_0)\|_2^2$ is the baseline misfit of the original solution, is selected following the discrepancy principle (*70, 71*). This criterion ties model complexity directly to the noise level. The group size L is varied over $\{5, 10, 15, \ldots, 70\}$ s to confirm that the set of active windows is stable with respect to the choice of group boundary (fig. S3).

To further quantify the contribution of each active group, we perform a leave-one-out (LOO) test: for each active group g, we remove it, refit the remaining groups, and measure the misfit increase $\Delta\chi^2_g = \chi^2_{\mathrm{LOO}}(g) - \chi^2_{\mathrm{selected}}$. A large $\Delta\chi^2_g$ indicates that group g is required by the data; a small value suggests it is marginal. The same LOO framework is also used to test the necessity of the MT and SF source types: all six MT components or all three SF components are removed from the group-sparse solution, the remaining components are refitted, and the resulting χ^2 increase quantifies the unique contribution of the removed source type (fig. S3).

Synthetic recovery tests

To assess whether the source features recovered from the real data—particularly the quiet-period signals and the implosion–explosion cycling—could be artifacts of the inversion procedure, we perform three synthetic recovery tests. In each test, a prescribed input source is used to generate synthetic waveforms through the actual Green's function kernels and station geometry employed in the real-data inversion. Gaussian random noise, scaled to the pre-P noise standard deviation measured at each station, is added to the synthetic data. The noisy synthetics are then passed through the identical inversion pipeline, and the recovered source time functions are compared against the known input (fig. S6).

Test 1: Full nine-component recovery. The input source is the optimum nine-component solution obtained from the real-data inversion, used in its entirety across the full time axis (t = 0–450 s). This test evaluates whether the inversion procedure faithfully recovers a complex, multi-episode source containing both eruptive and quiet-period signals at realistic noise levels. The recovered nine-component time functions reproduce the input across both eruptive and quiet-period intervals, including the low-amplitude M_{rt} and F_t signatures during the quiet period.

Test 2: Eruptive episodes only. The input source retains only the eruptive-episode portions of the optimum solution (Episodes 1–4), with all source amplitudes during the quiet period ($t \approx$ 50–210 s) set to zero for all nine components. Only the positive isotropic components (M_{rr}, M_{tt}, M_{pp}) are retained during the eruptive episodes. This test addresses a specific concern: whether the quiet-period signals observed in the real-data inversion could be generated as spectral leakage or temporal smearing of the large-amplitude eruptive pulses. The recovered quiet-period amplitudes remain at the level of the added noise, confirming that eruptive-episode energy does not leak into the quiet period through the inversion.

Test 3: Quiet-period deviatoric and horizontal-force components only. The input source retains only the deviatoric moment tensor components (M_{rt}, M_{rp}, M_{tp}) during the quiet period ($t \approx$ 50–210 s). All isotropic components and the single forces are set to zero across the entire time axis, and all components are set to zero outside the quiet period. This test evaluates whether the inversion can recover the specific source processes that we interpret as persistent shear deformation during the quiet period, in the absence of any eruptive-episode energy. The recovered deviatoric components closely track the input amplitudes well above the added noise level, while the isotropic and single-force components remain at noise level, confirming both the resolvability of low-amplitude shear deformation and the absence of cross-talk from other source types. A complementary resolution-matrix analysis of the moment-tensor–single-force separability is given in the Supplementary Text S2 and fig. S8.

Quiet-period decay analysis

The nine-component source time functions recovered from the Hunga eruption show nonzero amplitudes during the ~160 s quiet period. A natural concern is whether this quiet-period signal reflects a genuine ongoing source process or merely passive post-eruptive relaxation. To address this quantitatively, we fit the instantaneous amplitude envelope of each source component over the quiet period ($t = 50$–210 s) to three competing models of increasing complexity and select among them using the Bayesian Information Criterion (BIC) (fig. S7).

For each of the nine source components $s_m(t)$, we compute the analytic signal via the Hilbert transform and take the instantaneous amplitude envelope $E_m(t) = |s_m(t) + i\,\mathcal{H}\{s_m\}(t)|$, where $\mathcal{H}$ denotes the Hilbert transform. Both are computed on the full time series and then restricted to the quiet period. The envelope is smoothed with a uniform (boxcar) moving-average filter of width w; we test $w = 10$–40 s in 5 s increments to assess sensitivity, and classify a result as robust only when the preferred model is consistent across all window widths.

We consider three models for the smoothed envelope $E_m(t)$ over $t \in [50, 210]$ s (shifted to $t' = t - 50$ for fitting). Model F (Flat) assumes a constant amplitude $E(t') = c$ with one free parameter, representing a source component that neither decays nor grows during the quiet period. Model A (Exponential decay) assumes monotonic decay $E(t') = a\ \exp(-t'/\tau) + c$ with three free parameters, corresponding to the null hypothesis of passive post-eruptive relaxation with characteristic timescale τ. Model B (Piecewise: decay → growth) introduces a breakpoint t_b separating an initial decay from a subsequent re-acceleration, with six free parameters:

$$E(t') = \begin{cases} a_1\ \exp\!\big(-t'/\tau_1\big) + c, & t' < t_b, \\ a_2\ \exp\!\big(+(t' - t_b)/\tau_2\big) + c, & t' \geq t_b. \end{cases} \tag{S8}$$

The breakpoint t_b is determined by grid search over 5 s increments from $t' = 20$ to 135 s, selecting the value that minimizes the residual sum of squares. All other parameters are estimated by nonlinear least-squares fitting. Model selection uses the BIC $= n_{\text{eff}}\ \ln(\text{RSS}/n) + k\ \ln(n_{\text{eff}})$, where $n = 160$ is the number of envelope samples, k the number of free parameters ($k_F = 1$, $k_A = 3$, $k_B = 6$), and $n_{\text{eff}} = 16$ the number of independent samples, set by the shortest period in the inversion band; the model with the lowest BIC is preferred.

Across all seven smoothing widths, four components (M_{rr}, M_{tt}, M_{pp}, and F_r) prefer the piecewise model and two (M_{rt} and F_t) prefer the flat model: the volumetric and vertical-force components decay and then re-accelerate within the quiet period, whereas ring-fault shear and horizontal mass transport persist at Episode 1-level amplitudes without significant decay. The remaining three components (M_{rp}, M_{tp}, and F_p) shift their preferred model with smoothing width and are not interpreted. The breakpoint under Model B falls at $t \approx 170$–185 s but moves to $t \approx 70$–120 s if continuity is imposed at t_b, and is likewise not interpreted; the interpretation rests only on the component-selective character of the decay. Model A contains Model F as the limiting case $a \to 0$; for M_{rt} and F_t the fit collapses onto this limit, so τ is unconstrained, which is itself evidence that they do not decay. Where τ is identifiable it ranges from $\tau \approx 2$–9 s (F_r) through $\tau \approx 12$–16 s (isotropic components) to $\tau \approx 78$–176 s (M_{rp}); a single passive relaxation mechanism would impose a common timescale, and the observed spread of more than an order of magnitude rules this out. Taken together, the piecewise behavior of the volumetric and vertical-force components, the persistent flat behavior of ring-fault shear and horizontal force, and the absence of a common relaxation timescale demonstrate that the quiet-period source signal is not a passive artifact of Episode 1 but reflects ongoing, component-selective source activity during which different physical processes follow distinct temporal trajectories.

Onset timing sensitivity analysis

The ~5–10 s delay of F_r relative to M_{iso} at the onset of Episode 1 is reported in the main text as a potentially meaningful observation, but one that approaches the lower bound of the inversion passband (10 s period) and therefore requires careful assessment. We evaluate the robustness of this delay through a threshold-sensitivity test in which the onset time of each component is defined as the first time at which its absolute amplitude exceeds $n\sigma$, where σ is the standard deviation of the absolute amplitude measured during the period where the M_{iso} and F_r are apparently decreased (t = 80–170 s) and n is varied systematically over the range $n \in \{2, 3, 4, 5, 7, 10, 15, 20\}$. For each threshold $n\sigma$, we identify the exceedance time $t^e_{M_{\mathrm{iso}}}$ and $t^e_{F_r}$ within the Episode 1 window ($t = -10$ to 60 s) and within the Episode 2 window (t = 170 to 260 s), and compute the delay $\Delta t = t^e_{M_{\mathrm{iso}}} - t^e_{F_r}$, where negative values indicate that M_{iso} leads F_r (fig. S5).

For Episode 1, Δt is dominantly negative across the tested thresholds from $n = 2$ to $n = 10$, ranging from +1 s to −10 s, indicating that M_{iso} systematically exceeds the threshold before F_r. At higher thresholds (n = 15, 20), Δt becomes slightly positive, but these thresholds approach the peak amplitude of the signal, where the exceedance time is sensitive to the exact waveform shape near the maximum and is therefore less reliable as an onset indicator. The robust range of $n = 3$–10σ yields $\Delta t \approx -5$ to -10 s for Episode 1. For Episode 2, Δt fluctuates around zero across all tested thresholds, with values ranging from −5 to +4 s with no systematic sign. This indicates that M_{iso} and F_r onset near-simultaneously at the beginning of Episode 2, with any apparent lead or lag within the uncertainty of the measurement. The contrast between Episodes 1 and 2 is robust to the choice of threshold: M_{iso} leads F_r by ~5–10 s in Episode 1 across a wide range of $n\sigma$, whereas no systematic lead is observed in Episode 2. We note that the quiet-period window (t = 80–170 s) used to define σ was chosen to avoid both the coda of Episode 1 and the onset of Episode 2. The results are not sensitive to modest changes in this window (e.g., using t = 60–150 s or t = 100–200 s produces consistent Δt values).

Frictional plug release

The failure overpressure inferred from the peak vertical single force can be reached by either of two mechanisms. It falls within the tensile strength of andesitic volcanic rocks, 7–11 MPa (*33*). It is also consistent with frictional release of a plug overlying the sealed volume (*34–36*). A vertical force due to the overpressure acting at the bottom of the plug, $\pi r_c^2 \Delta P$, is balanced by the frictional resistance on the sidewalls, $2\pi r_c H \tau$, where H and r_c are the plug height and radius, respectively, and τ is the average shear stress acting at the plug walls. Assuming that the normal stress σ_n acting at the plug walls is lithostatic, shear failure will initiate when $\tau = \mu(\sigma_n - p)$, where μ is the coefficient of friction, and p is the pore fluid pressure. Integrating the failure shear stress over depth gives $\mu \Delta\rho g/2$, where $\Delta\rho$ is the density contrast between the rock and the pore fluid (assuming hydrostatic fluid pressure) and g is the gravitational acceleration. The force balance thus provides a limit on the overpressure acting at the bottom of the plug:

$$\Delta P = \mu\, \Delta\rho\, g\, \frac{H^2}{r_c}. \tag{S9}$$

For physically plausible conduit-scale plug dimensions (r_c = 50–200 m, H = 100–1000 m, $H/r_c \leq 10$, $H^2/r_c \leq 2000$ m), $\Delta\rho \approx 1500$ kg m^{-3}, and μ = 0.4–0.6 (*14, 15, 37, 38*), Eq. (S9) yields ΔP of the order of 0.1–10 MPa (Fig. 3). The upper bound on H^2/r_c is set by the requirement that frictional release occur before the caldera roof fails in tension or by slip on the bounding ring faults. We point out that the overpressure suggested by Eq. (S9) implies a uniform failure along the cylindrical plug wall. In case of a partial failure such as that envisioned by the trapdoor mechanism (*13, 14, 72*), the critical overpressure may be reduced by a factor of ~2. Assuming representative parameters of the Hunga plug (H = 400 m, r_c = 100 m, μ = 0.6) gives rise to $\Delta P \approx 7$ MPa, matching the seismically inferred value. Other factors that may lower the estimated

ΔP include above-hydrostatic pore pressures (e.g., due to percolation of phreatomagmatic fluids in the fault zone) and stress concentration around the tips of incipient shear cracks at the plug walls. Note that Eq. (S9) applies to both the conduit plug and the caldera roof, with the appropriate choice of the height and radius. The same r_c sets V_{eff} in Eq. (2) of the main text, whereas the caldera radius r sets the coupling area in Eq. (1). The sealed volume that is re-pressurized is therefore much smaller than the roof across which its overpressure acts, and the two scales are complementary rather than exclusive.

Sealed-volume recharge

Equation (2) of the main text follows from treating the sealed region as a fixed volume V_{eff} containing a compressible fluid of bulk modulus K. Injecting volume at a rate Q raises the pressure at $\mathrm{d}P/\mathrm{d}t = KQ/V_{\text{eff}}$, so the overpressure grows linearly with time and reaches ΔP_{fail} after $t_{\text{fail}} = \Delta P_{\text{fail}} V_{\text{eff}}/(KQ)$. We adopt $K = 0.5$ GPa, appropriate for bubble-bearing magma (*23, 31*); for a bubbly fluid the compressibility of the contained magma greatly exceeds that of the confining rock, so K is set by the fluid rather than by the chamber walls. Constant Q over the recharge interval is an idealization; a monotonically increasing Q would shorten t_{fail} for the same V_{eff} and would not change the conduit-scale identification, which depends on the ratio V_{eff}/Q rather than on either quantity alone.

Here Q is the local rate at which magma and phreatomagmatic steam enter the sealed region, and is distinct from the long-term deep magmatic supply rate. The steam-dominated plume inferred for the climactic phase (*8*) establishes that magma–seawater interaction was intense, but it does not localize where that interaction occurred: the mixing may have taken place at depth through induced fuel–coolant interaction, or at the sea surface as pyroclastic density currents entered the ocean (*8*). Only the former contributes to Q. We therefore do not use the plume inference to estimate Q directly. The recharge flux is instead constrained by the recurrence timescale itself, through the ratio $V_{\text{eff}}/Q \approx 10^4$ s required by Eq. (2); the plume observation enters only as evidence that a submarine andesitic system can sustain local inflow rates far above its deep magmatic supply.

Tsunami simulation

We compiled a topo-bathymetric grid from the highest-resolution source available in each region: the Tongatapu shallow-water compilation (*73, 74*), the pre-eruption Hunga DEM (*75*), and GEBCO_2026 (*76*) elsewhere. Rather than merging the gridded products, we combined the pre-gridded point datasets, retaining only the Tongatapu shallow-water points from Borrero et al. (*73*) so that the higher-resolution Hunga DEM and GEBCO_2026 could replace the lower-resolution offshore soundings. Points on the pile-supported Vuna Wharf were removed, as the DEM rendered the wharf as land and would otherwise block propagation. Overlapping points were culled with a KD-tree (`scipy.spatial.cKDTree`), and a wide transition zone was used at the northern Borrero–GEBCO boundary to avoid an artificial bathymetric gradient. The merged points were interpolated with GMT6 `surface` (tension 0.25) on a grid three times finer than the target and resampled, yielding two nested grids at 3 arcsec (~90 m, full domain) and 1 arcsec (~30 m, Tongatapu). We compared against the tide-gauge record from Queen Salote Wharf, Nuku'alofa (*62, 77*). The gauge measures the sea level every second and records one value per minute, the average over the preceding minute; the first value after the eruption onset (04:14:45 UTC) was subtracted to remove the offset.

We solved the non-linear Boussinesq equations with JAGURS v0601 (*78*), with a time step of 0.2 s to satisfy the CFL condition, a Manning roughness coefficient of 0.025, and dispersion enabled throughout. The initial sea-surface displacement follows the impulsive-explosion model of Le Méhauté (*79*), an axisymmetric profile with a central depression and an elevated rim,

$$\eta(r) = \begin{cases} \eta_0 \left[2 \left(\frac{r}{R} \right)^2 - 1 \right], & r < R, \\ 0, & r > R, \end{cases} \tag{S10}$$

centered at 175.387°W, 20.5532°S, with effective radius $R = 3$ km and peak amplitude $\eta_0 = 100$ m. A Gaussian filter ($\sigma = 0.1R$) removed the discontinuity at $r = R$, after which the source spanned surface displacements of −96 to +48 m. This source is a kinematic representation of the sea-surface disturbance generated by each explosive episode; its lateral scale characterizes the surface water displacement, and is neither the dimensions of the sealed volume at depth nor the caldera radius. To isolate the role of the recovered timing, we held this spatial source and its amplitude fixed and varied only the source-time function, each activation ramping linearly from zero. Three scenarios were tested (fig. S9): (1) a single activation over 0–50 s; (2) six consecutive activations at 50-s intervals over 0–300 s; and (3) an activation over 0–50 s, a quiescent interval from 50 to 200 s, and two further activations over 200–250 s and 250–300 s, approximating the seismically resolved quiescence. Because every scenario uses an identical spatial source and amplitude, the comparison depends on the source timing alone and not on any assumed amplitude ratio between episodes.

Synthetic waveforms were output at Queen Salote Wharf (21.1378°S, 175.1813°W) and compared both directly and after a 60-s moving average evaluated at the gauge logging times, mimicking the instrumental averaging described above. Prior modeling of this record noted that closer agreement would require a more complex source than a single idealized explosion (*7*). The comparison here targets the multiplicity and relative timing of the wave peaks, not their absolute arrival times or amplitudes, and no source inversion is performed. Absolute arrival times are not expected to be predictive, because the path traverses the extended shallow shelf north of Tongatapu, where the travel time is acutely sensitive to bathymetric uncertainty, and because the eruption itself altered the near-source bathymetry (*9*). Among the three scenarios, the single and uninterrupted ones each produce one dominant wave packet, as arrivals from the 50-s-spaced activations overlap and are smoothed by the gauge averaging, whereas the scenario with the quiescent interval produces multiple separated peaks with spacing comparable to the observed sequence.

Supplementary Text

Text S1: Reduced-component tests

We assess whether the deviatoric moment-tensor components are independently required by the data by re-running the group-sparse inversion with the moment tensor restricted to its isotropic part and with the three single-force components allowed to be free. Under this restriction, the six moment-tensor components in the source representation collapse to the single scalar M_{iso} acting on δ_{ij}, so that the total source representation reduces from nine components to four (M_{iso}, F_r, F_t, F_p). The remaining components are refit on the support selected by the group-sparse procedure (*21*).

Table S1 summarizes the misfit increase for this configuration alongside the reported ablations (MT-only, SF-only; fig. S3). The unconstrained solution $\mathbf{s}_0$ yields $\chi^2_{\text{base}} = 1.50 \times 10^4$, so the discrepancy-principle threshold is $\chi^2_{\text{threshold}} = 1.10\,\chi^2_{\text{base}} = 1.65 \times 10^4$; the selected full nine-component group-sparse model refits to $\chi^2_{\text{selected}} = 1.35 \times 10^4$ (*21*). Restricting the moment tensor to its isotropic part while keeping the three single-force components free (“ISO + 3 SF”) yields a refit $\chi^2 = 1.77 \times 10^4$, which corresponds to a 31%

increase relative to χ^2_{selected}. The model therefore fails the discrepancy criterion, indicating that the deviatoric components of the moment tensor are independently required by the data and cannot be absorbed into the isotropic and single-force representation.

The pure MT-only and SF-only configurations fail by very large margins (+86% and +143%, respectively), demonstrating that the data require both moment-tensor and single-force contributions. The ISO + SF configuration is the best-fitting reduced subset, indicating that the volumetric and single-force components together carry the largest share of the source signal. Two further configurations isolate this contribution. Retaining the isotropic moment alone ("ISO only") yields +111%; adding the three single forces reduces this to +31%, and adding the deviatoric components in turn recovers the full model, confirming that neither source type substitutes for the other. The converse restriction, retaining the deviatoric moment tensor with the single forces but removing the isotropic moment ("Deviatoric + 3 SF"), yields +106%. The source is dominated by its volumetric part, yet the markedly smaller ISO + 3 SF deficit (+31%) relative to this converse (+106%) shows that the deviatoric radiation, though subordinate, is not redundant with M_{iso} and the single forces.

Text S2: Separability of the moment tensor and single force

The joint recovery of moment-tensor and single-force time histories warrants scrutiny, because the two representations can be difficult to separate. Day and McLaughlin (*80*) showed that when the point force and moment tensor describe a single source and are therefore linked by a fixed, instantaneous proportionality, as for a spall source, the two representations are equivalent and their simultaneous inversion is singular. For the 2022 Hunga eruption specifically, Garza-Girón et al. (*19*) found that the eruptive reaction force, an isotropic implosion, and ring-fault slip produce nearly indistinguishable long-period radiation, and Thurin & Tape (*18*) obtained comparable fits with either a force or a moment-tensor source when each subevent was represented by a single short impulse. These non-uniqueness results share a common premise, and the force and moment tensor are either tied by a fixed proportionality (*80*) or parameterized by identical, simple time functions and compared as alternatives (*18, 19*). Our inversion does not operate in that regime. We solve for the six moment-tensor and three single-force components simultaneously as independent, continuous time functions, and the recovered $M_{\text{iso}}(t)$ and $F_r(t)$ evolve differently rather than in proportion (Fig. 2 of the main text; fig. S2).

We assess the separability of the two source types with the model resolution matrix. Let $\mathbf{G}$ be the forward operator mapping the source time histories to the data, $\mathbf{W}$ the noise whitening operator (a diagonal matrix of the reciprocal pre-event noise standard deviation at each station), and $\mathbf{S}$ a diagonal source-amplitude scaling whose entries normalize each component by the Euclidean norm of the corresponding unconstrained solution $\mathbf{s}_0$, so that all nine components are comparably scaled. Writing the whitened, column-scaled forward operator as $\tilde{\mathbf{G}} = \mathbf{WGS}$ and α for the Tikhonov parameter of the refit (*21*), the resolution matrix is

$$\mathbf{R} = \left(\tilde{\mathbf{G}}^\top \tilde{\mathbf{G}} + \alpha \mathbf{I}\right)^{-1} \tilde{\mathbf{G}}^\top \tilde{\mathbf{G}}, \tag{S11}$$

so that the recovered model relates to the true model by $\hat{\mathbf{s}} = \mathbf{R}\,\mathbf{s}_{\text{true}}$. The rows and columns of $\mathbf{R}$ are indexed by (component, time), with the nine components ordered as the six moment-tensor components followed by the three single-force components. For a given time sample t, let $\mathcal{M}(t)$ denote the six row/column indices of the moment-tensor components at that time and $\mathcal{F}(t)$ the three indices of the single-force components. We define the same-time self-resolution and cross-talk blocks

$$\rho_{\mathrm{MT}}(t) = \left\|\mathbf{R}[\mathcal{M}(t), \mathcal{M}(t)]\right\|_F, \qquad \rho_{\mathrm{SF}}(t) = \left\|\mathbf{R}[\mathcal{F}(t), \mathcal{F}(t)]\right\|_F, \tag{S12}$$

$$c_{\mathrm{MT}\to\mathrm{SF}}(t) = \left\|\mathbf{R}[\mathcal{F}(t), \mathcal{M}(t)]\right\|_F, \qquad c_{\mathrm{SF}\to\mathrm{MT}}(t) = \left\|\mathbf{R}[\mathcal{M}(t), \mathcal{F}(t)]\right\|_F, \tag{S13}$$

where $\| \cdot \|_F$ is the Frobenius norm and $\mathbf{R}[\mathcal{A}, \mathcal{B}]$ is the submatrix of $\mathbf{R}$ with rows $\mathcal{A}$ and columns $\mathcal{B}$. Here $c_{\mathrm{MT}\to\mathrm{SF}}(t)$ measures the leakage of the true moment tensor into the recovered single force at the same time sample, and $c_{\mathrm{SF}\to\mathrm{MT}}(t)$ the converse. We report these leakages normalized by the corresponding self-resolution, $c_{\mathrm{MT}\to\mathrm{SF}}(t)/\rho_{\mathrm{SF}}(t)$ and $c_{\mathrm{SF}\to\mathrm{MT}}(t)/\rho_{\mathrm{MT}}(t)$, so that a value well below unity indicates that the recovered amplitude of one source type is not an artifact of leakage from the other. Throughout the climactic phase (t =0–300 s), the moment-tensor and single-force self-resolutions remain stable and well separated from zero, and the same-time cross-talk ratios stay at a few per cent (below ∼5% through the eruptive episodes, rising to ∼6% late in the sequence as the single-force self-resolution declines; fig. S8). The recovered single force is therefore not an artifact of moment-tensor leakage, nor the moment tensor an artifact of the single force.

Text S3: Comparison with previous single-force inversions

Three previous source analyses of the 2022 Hunga eruption have reported a net downward vertical single force for the climactic phase (*18, 19, 81*). Hu et al. (*20*) reported an upward vertical force for the first major event using a joint moment-tensor and single-force inversion, but interpreted it as a water-column rebound. Our result is consistent in sign with Hu et al. (*20*) but assigns a different physical mechanism. It is in apparent contradiction with the downward reports of the three earlier studies, but this contradiction is resolved once the methodological differences are made explicit.

The bipolar structure of $F_r(t)$ as the source of the apparent disagreement. The recovered $F_r(t)$ is not monotonically positive. It begins each eruptive episode with a small-amplitude negative excursion (downward force, of order several $\times 10^{13}$ N), then rises through zero to a large positive peak of order 10^{14} N (upward force), and returns to a negative excursion before the next cycle (fig. S2). The same negative-then-positive sequence appears at the onset of every episode and is also visible in the unfiltered broadband records as a coherent negative first motion followed by the main explosive arrival (fig. S4). The single-force signal of the Hunga eruption is therefore intrinsically bipolar in time.

Garza-Girón et al. (*19*) impose a positivity constraint $F_z(t) \geq 0$ in the downward direction during the climactic-phase deconvolution; only one sign of the force can appear in the solution, and the negative-then-positive structure is collapsed onto the negative half by construction. The sign-free deconvolutions in Garza-Girón et al. (*19*) address a different signal. Their unconstrained deconvolution (their Fig. 8) targets the post-climactic atmospheric standing-wave forces (peak amplitude $\sim 4 \times 10^{12}$ N), and their positivity-constrained surface-wave deconvolution extends the reaction-force history out to ∼16,000 s (their Figs. 5–6). Neither replaces a sign-free reconstruction of the climactic-phase P-wave episodes that constitute the present comparison, for which they impose the downward positivity constraint. Thurin & Tape (*18*) represent each subevent as a single Gaussian impulse of ∼1 s duration; an impulse of fixed sign cannot represent a bipolar oscillation, and whichever sign dominates the integrated waveform fit becomes the sign of the impulse. Poli & Shapiro (*81*) assume a downward reaction-force model from the outset. In all three cases, the parameterization treats the single-force time history as effectively monochromatic in sign, and the negative half of the bipolar oscillation is absorbed into the reported downward solution while the positive half is not represented.

Polarity from the unfiltered records. Thurin & Tape (*18*) state explicitly that "a downward point force source would produce positive (upward) first arrivals on seismograms, while an upward point force source would produce negative (downward) first arrivals." They also state that origin-time uncertainty larger than 10 s introduces a cycle-skipping ambiguity that makes upward and downward solutions nearly equivalent in their grid search (their Fig. 4e). Applied to the coherent negative first motions in our unfiltered records (fig. S4), the polarity convention stated by Thurin & Tape (*18*) themselves requires the source force to be upward at the onset of the climactic phase, which is the sign recovered here and the sign that initiates the bipolar oscillation of $F_r(t)$. The polarity constraint from the unfiltered records is independent of the inversion result and is not subject to the cycle-skipping ambiguity discussed by Thurin & Tape (*18*).

Distinction from the water-column rebound mechanism. Hu et al. (*20*) recover an upward F_z for the first major event ($+2.0 \times 10^{13}$ N) in their joint MT+SF inversion, and report that an SF-only inversion of the same data yields a downward force of 4.8×10^{13} N; the joint inversion is therefore the basis of their sign reversal. The sign is consistent with our result. Their proposed physical interpretation, however, is that the upward force is the elastic rebound of the solid Earth in response to a transient drop in the seafloor pressure that follows the shallow submarine explosion, that is, an external loading mechanism in which the overlying water column responds to each seafloor pressure change and the solid Earth responds in turn.

Our solution is inconsistent with the water-rebound interpretation. An isotropic seafloor pressure drop drives an essentially vertical elastic response of the solid Earth, with negligible horizontal force and no source of deviatoric moment. We recover a persistent off-diagonal moment-tensor component M_{rt}, well constrained by the vertical-component P-wave radiation pattern, that retains most of its Episode 1 amplitude through the quiet period (50–210 s) after F_r and M_{iso} have decayed (figs. S2 and S7); the horizontal single force F_t, though less well constrained by the predominantly vertical station set, behaves the same way, and the envelope model selection identifies both M_{rt} and F_t as flat across the quiet period, in contrast with the decaying behavior of M_{iso} and F_r. A purely isotropic external loading by the water column cannot produce a horizontally asymmetric source signature that outlives the vertical signal. We note that coupled simulations of the 2018 Anak Krakatau flank collapse show that horizontal reaction forces from disturbed seawater contribute to seismic excitation (*82*); testing such a contribution for Hunga is beyond our scope, and any such contribution would not be separable from our horizontal force components.

We emphasize that the coupled M_{iso}–F_r behavior by itself does not discriminate between the two interpretations. The joint rise of the two components during each episode and their joint decay into the quiet period are reproduced by an internal overpressure cycle and by an external water-column response alike, because both are driven by the same seafloor pressure history. The discriminant is the deviatoric and horizontal radiation that persists after the vertical and volumetric signals have decayed, which the external mechanism cannot generate.

The physical mechanism behind the bipolar oscillation. The bipolar structure follows from the implosion–explosion staging of each episode described in the main text. The negative excursion at episode onset records the reaction to the upward mass-momentum transient that accompanies seal failure, and the trailing negative excursion records the deceleration of the downward-moving caldera roof as the cavity contracts and the next overpressure build-up begins; the intervening positive peak is the reaction to the downward mass redistribution discussed in the main text. The bipolar force history is therefore an expected consequence of the cyclic mechanism rather than an artifact of the inversion.

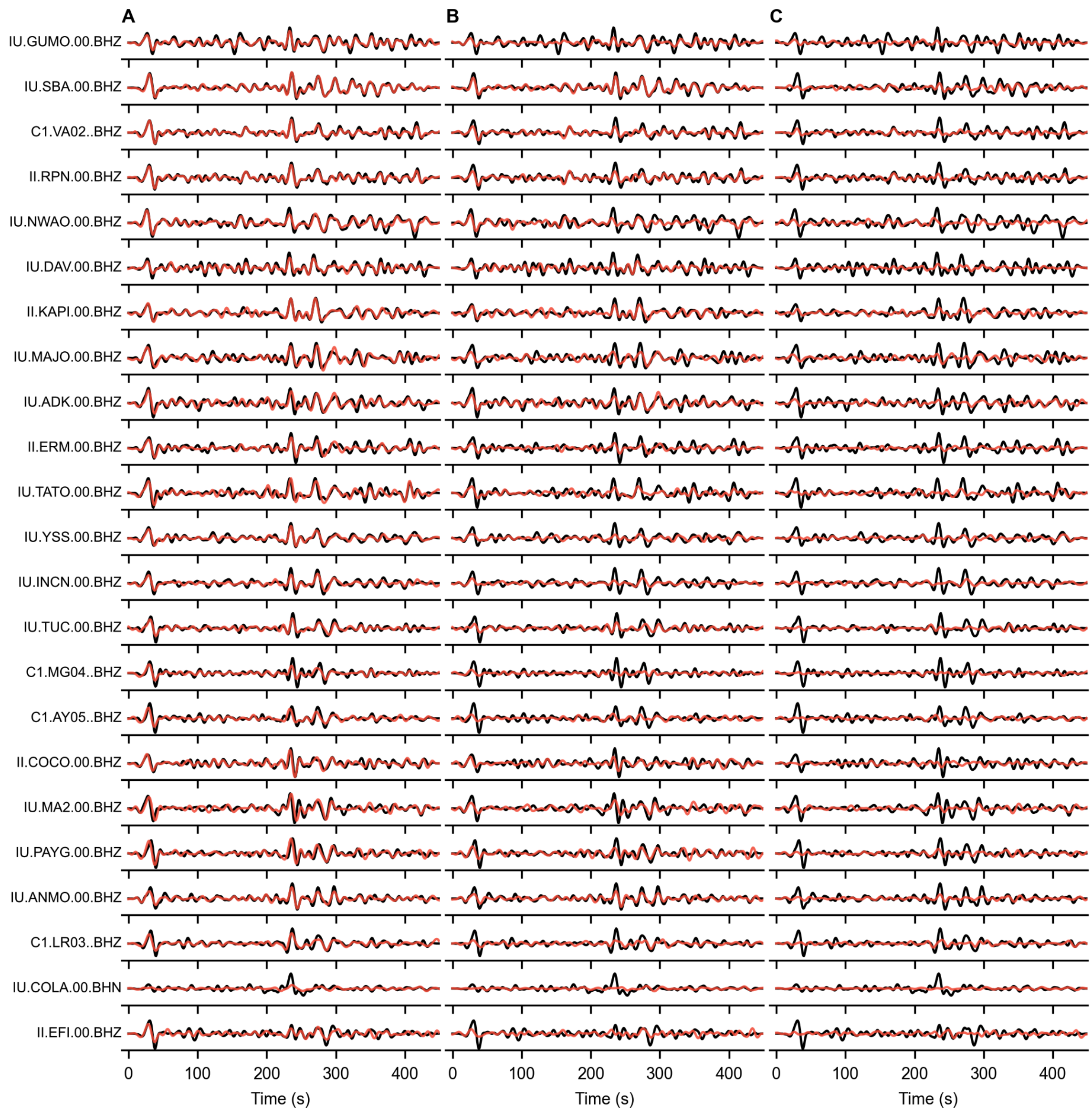

Figure S1: Waveform fits of the observed teleseismic records for three inversion configurations. (A) The composite nine-component inversion (full MT + SF), (B) inversion using only the six MT components, and (C) inversion using only the three SF components. The channel identifier is annotated to the left of each row in (A). Black traces are the observed records. Red traces are the predicted records from the corresponding inversion.

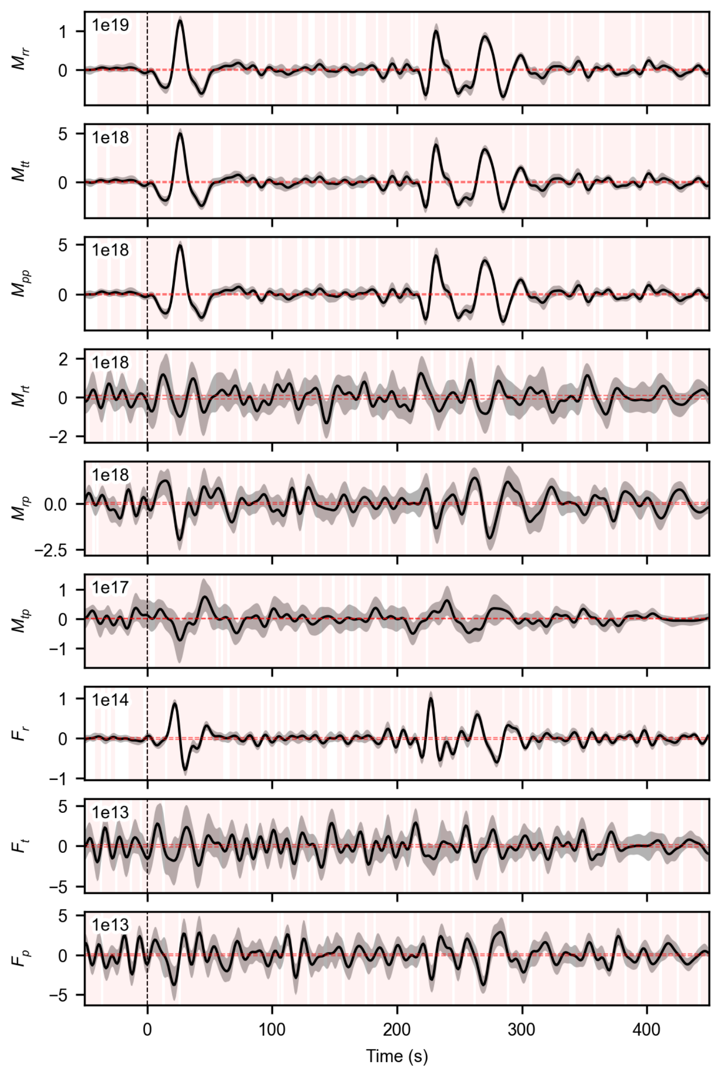

Figure S2: Nine-component source time functions with bootstrap confidence intervals and pre-event noise floors. Each panel shows one source component (top to bottom): the six moment tensor components (in N m) and the three single force components (in N). Black traces are recovered source time functions. Gray shading is a bootstrap 95% confidence interval from $N_B = 1000$ resampled inversions (*21*). Red dashed lines are pre-event noise floor $\pm\sigma_m^{\text{noise}}$ for each component (*21*). Light red shading are intervals where the absolute amplitude exceeds the noise floor. Vertical dashed line is the hypothesized event origin time.

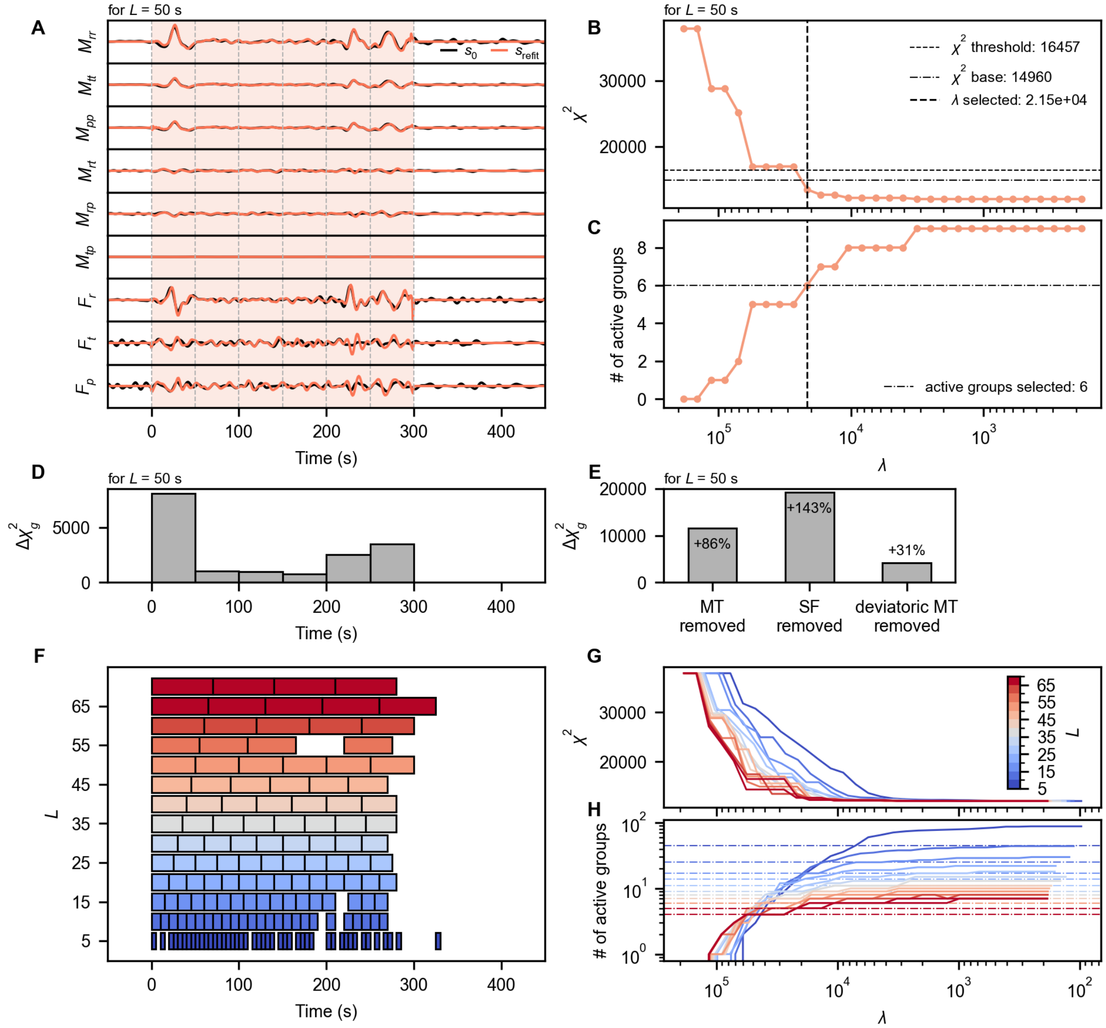

Figure S3: Group-sparse post-processing results. (A) Nine-component source time functions for $L = 50$ s. Black and red traces are the unconstrained and group-sparse refit solutions, respectively (*21*). The MT and SF components are scaled by the peak amplitudes of the M_{rr} and F_r components of s_0, respectively. Shaded intervals mark the active groups selected by the group-sparse solution. (B) χ^2 misfit along the λ path for $L = 50$ s. The vertical dashed line is the selected λ at which the sparsest model satisfying the discrepancy principle is obtained. (C) Number of active groups along the λ path for $L = 50$ s. (D) Leave-one-out misfit increase $\Delta\chi^2_g$ for each active group, computed by removing group g, refitting the remaining groups, and measuring the resulting χ^2 increase relative to the selected solution. (E) Leave-one-out misfit increase from removing source components from the group-sparse solution and refitting. (F) Active windows recovered for each L. The placement of active windows is consistent across L, confirming that the recovered set of active intervals is robust to the choice of group boundary. (G) χ^2 misfit along the λ path for all tested group sizes. (H) Number of active groups along the λ path for all tested L, with horizontal dash-dotted lines marking the number of active groups at the selected λ for each L.

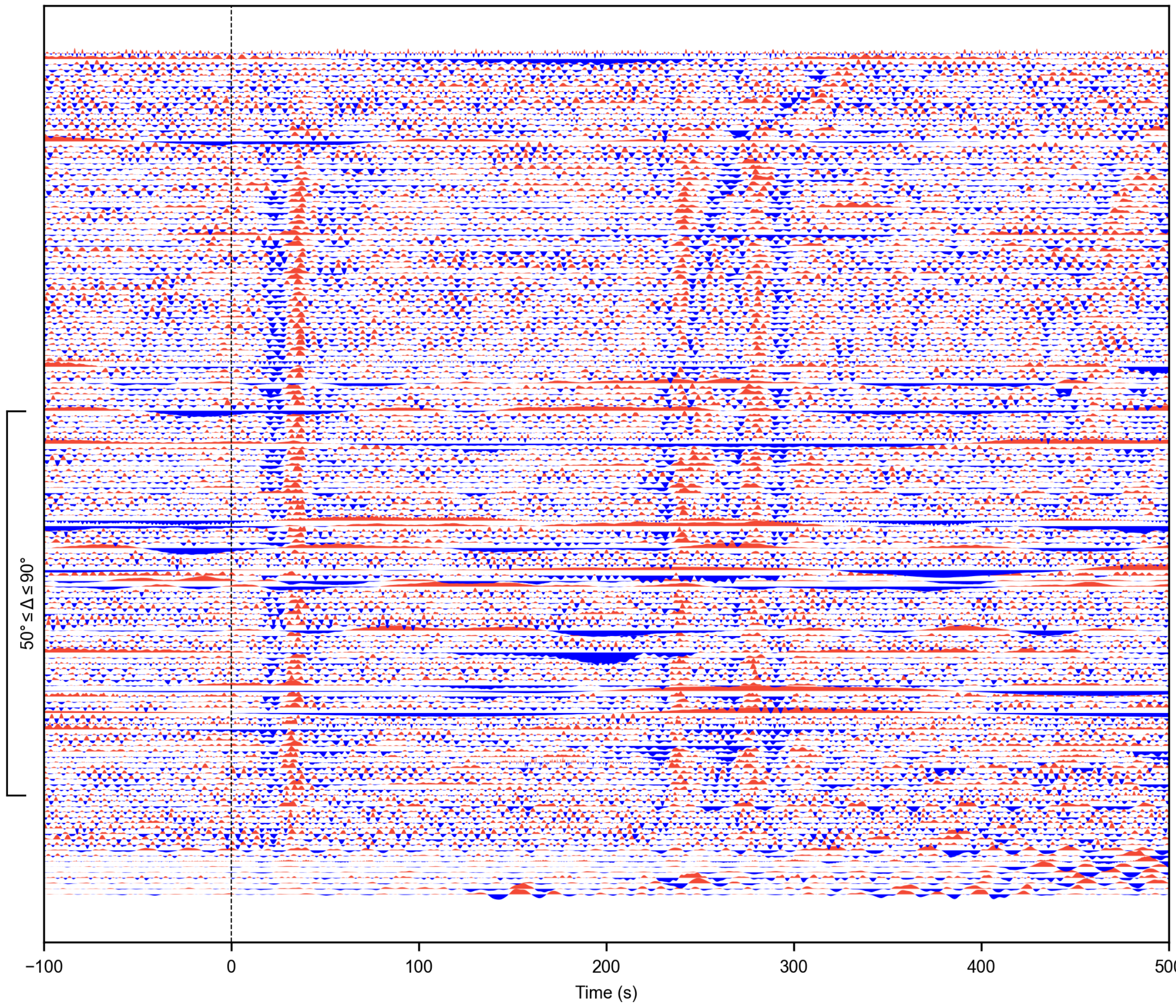

Figure S4: Unfiltered broadband vertical-component (BHZ) displacement records around the predicted P-wave arrival. Each trace is the displacement record at one station, plotted as a function of time relative to the predicted P-wave arrival ($t = 0$, vertical dashed line) and normalized by its peak absolute amplitude. Red and blue fills indicate positive and negative amplitudes, respectively. Traces are sorted by epicentral distance for stations within 0–120°. The bracket on the left marks the 50°–90° epicentral range used for the frequency-domain inversion. The coherent negative first motions across the network confirm the implosive onset of Episode 1 directly in the unfiltered records, prior to any processing.

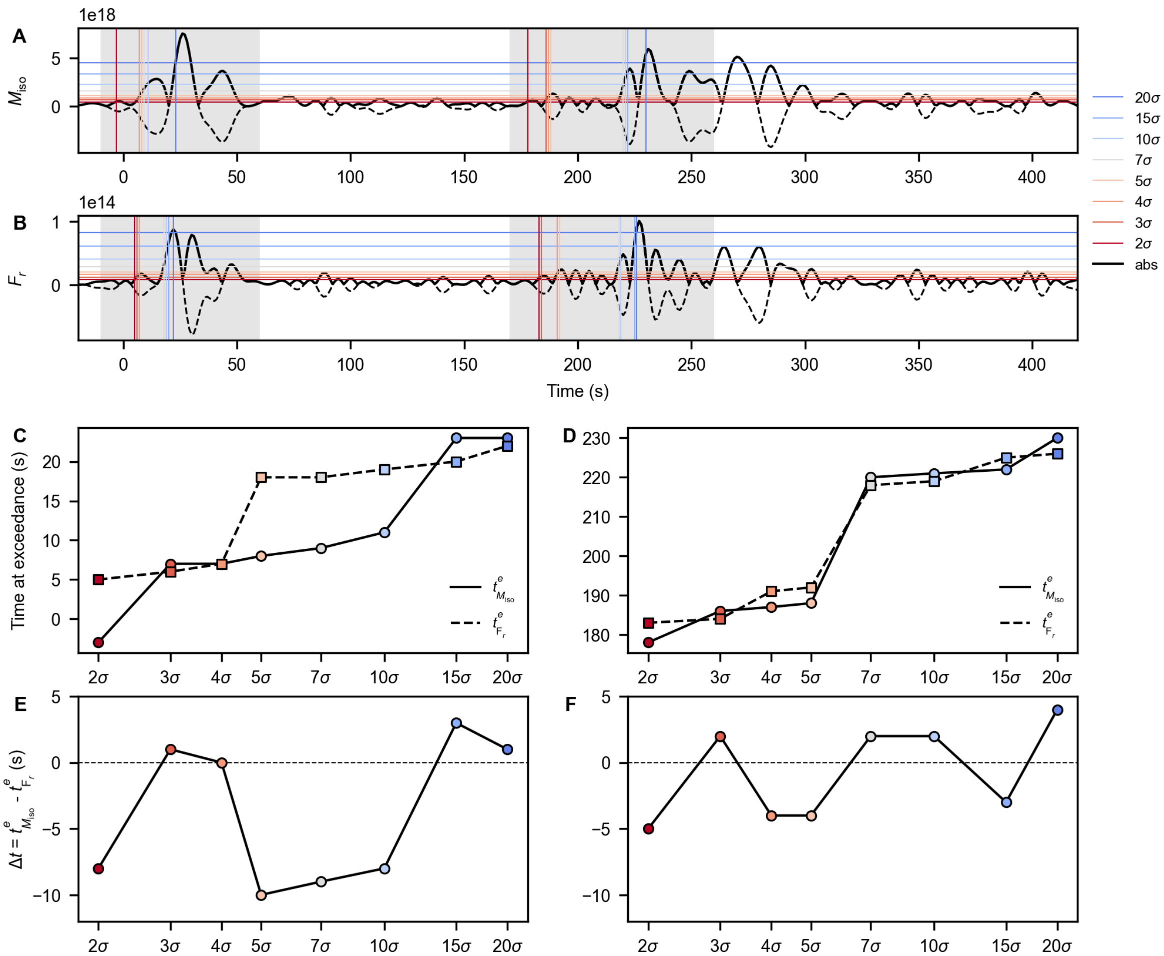

Figure S5: Threshold-sensitivity analysis of the onset timing of M_{iso} and F_r. (A) $M_{\text{iso}}(t)$ over the climactic phase. The dashed black trace is the time series and the solid black trace is its absolute value. Gray shaded intervals are the Episode 1 and Episode 2 windows within which the threshold-exceedance time $t^e_{M_{\text{iso}}}$ is searched. Horizontal colored lines are the $n\sigma$ thresholds for $n \in \{2, 3, 4, 5, 7, 10, 15, 20\}$, where σ is the standard deviation of $|M_{\text{iso}}|$ measured over $t = 80$–170 s. Vertical colored lines mark the corresponding $t^e_{M_{\text{iso}}}$ for each threshold within each episode window. (B) Same as (A), for $F_r(t)$. (C) Threshold-exceedance times $t^e_{M_{\text{iso}}}$ (circles) and $t^e_{F_r}$ (squares) for Episode 1 as a function of $n\sigma$. Marker color encodes n as in (A) and (B). (D) Same as (C), for Episode 2. (E) Onset delay $\Delta t = t^e_{M_{\text{iso}}} - t^e_{F_r}$ for Episode 1 as a function of $n\sigma$. Negative values indicate that M_{iso} exceeds the threshold before F_r. (F) Same as (E), for Episode 2.

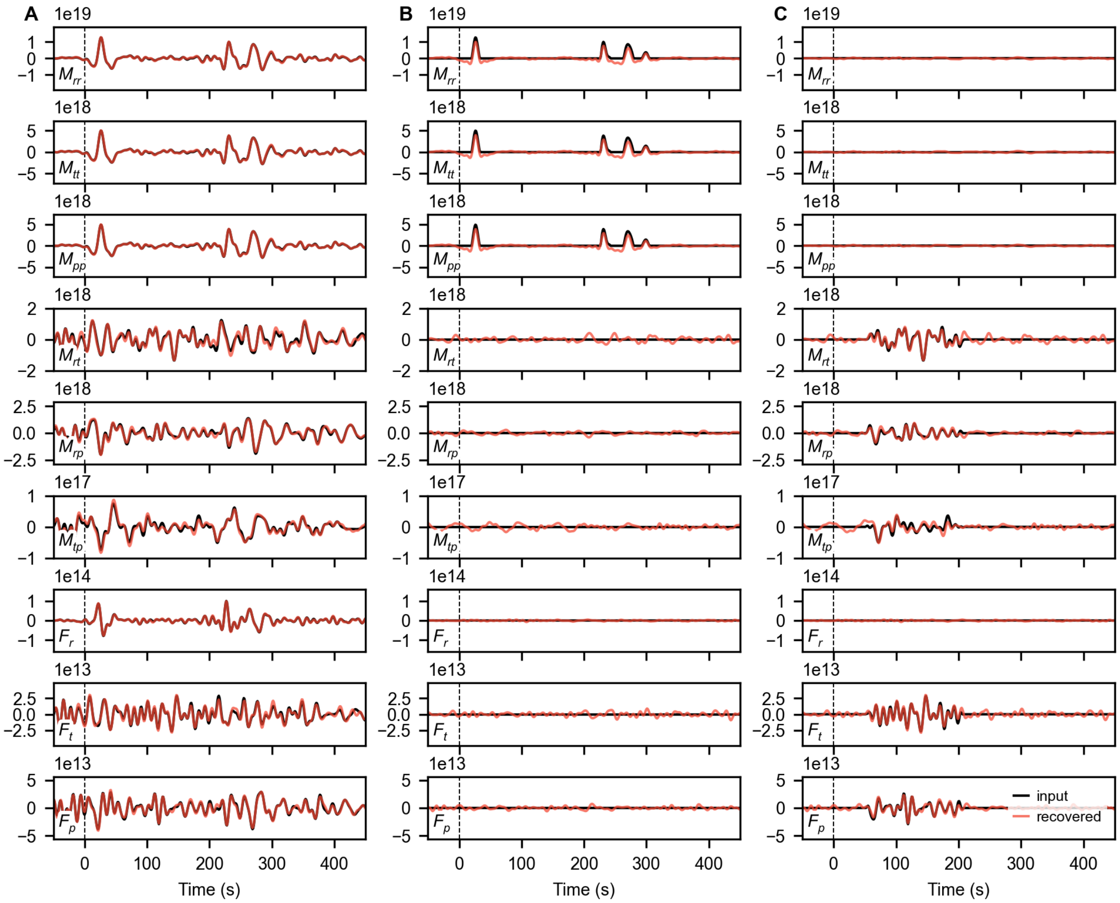

Figure S6: Synthetic recovery tests. (A) Full nine-component recovery. (B) Eruptive episodes only. (C) Quiet-period deviatoric and horizontal-force components only. Black traces are the input source. Red traces are the source recovered from the noisy synthetics for each test. Vertical dashed lines mark the hypothesized event origin time.

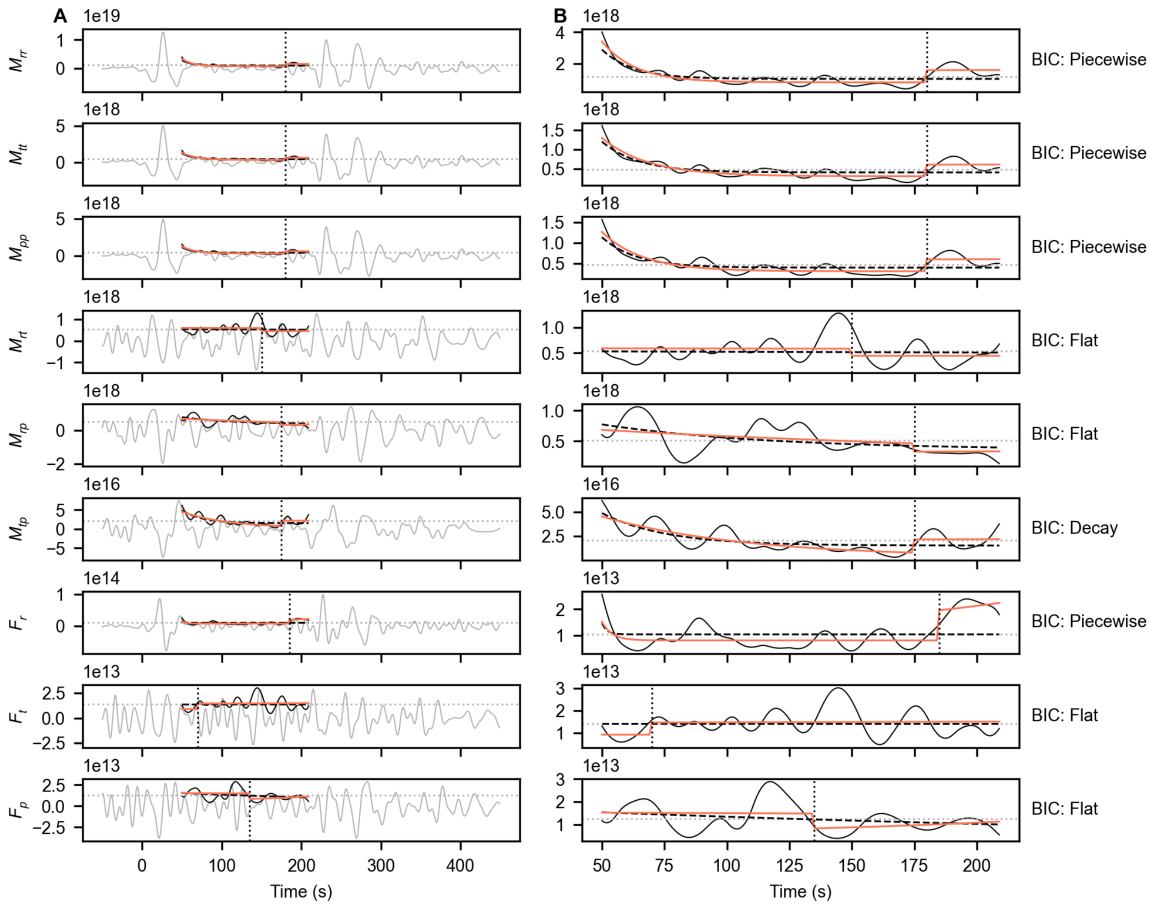

Figure S7: Envelope-based model selection for the quiet-period decay analysis. (A) Full time axis. Gray traces are the source time functions s_0 for each component. Black traces are the smoothed instantaneous amplitude envelopes, computed on the full time series and shown over the quiet period. Dotted horizontal lines are the flat model (Model F). Dashed black curves are the exponential decay model (Model A). Red curves are the piecewise decay-then-growth model (Model B); vertical dotted lines mark the breakpoint identified by grid search. (B) Same as (A), zoomed to the quiet period. The model preferred by BIC for each component is annotated to the right. Shown is the result for envelope smoothing width w = 10 s, and the best-fit parameters are given in (*21*).

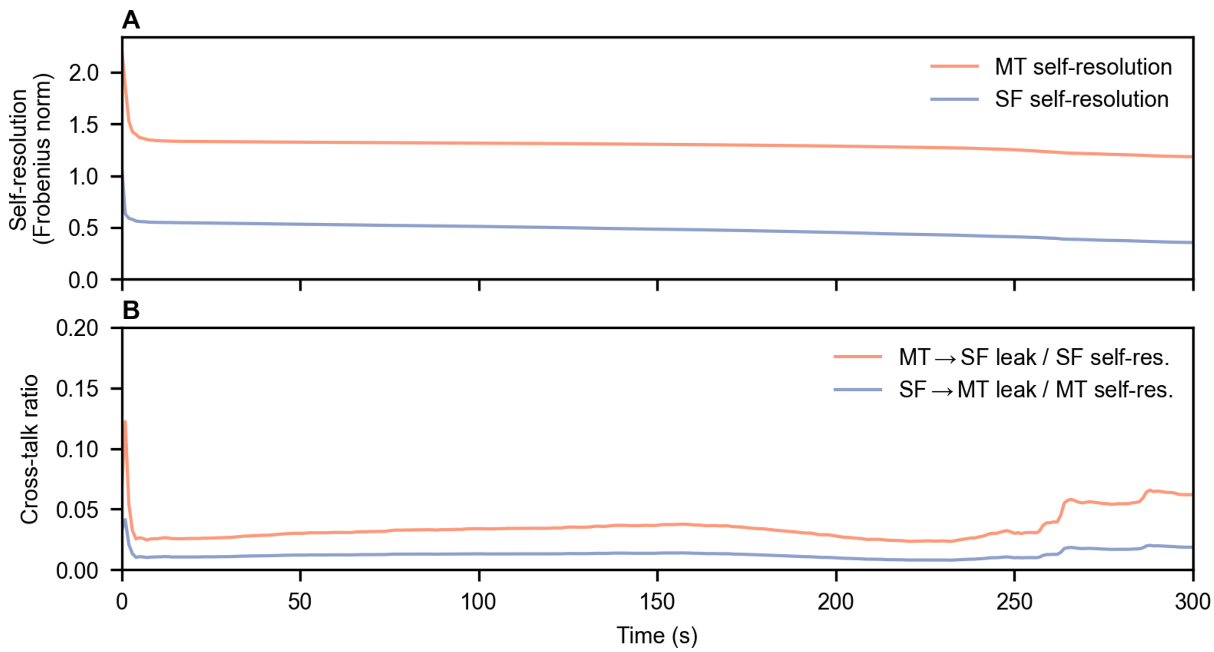

Figure S8: Resolution of the moment-tensor and single-force components. (A) Same-time self-resolution $\rho_{\mathrm{MT}}(t)$ and $\rho_{\mathrm{SF}}(t)$. (B) Same-time cross-talk ratios $c_{\mathrm{MT}\to\mathrm{SF}}/\rho_{\mathrm{SF}}$ and $c_{\mathrm{SF}\to\mathrm{MT}}/\rho_{\mathrm{MT}}$, which stay at a few per cent throughout the climactic phase, showing that the two source types are separately resolved.

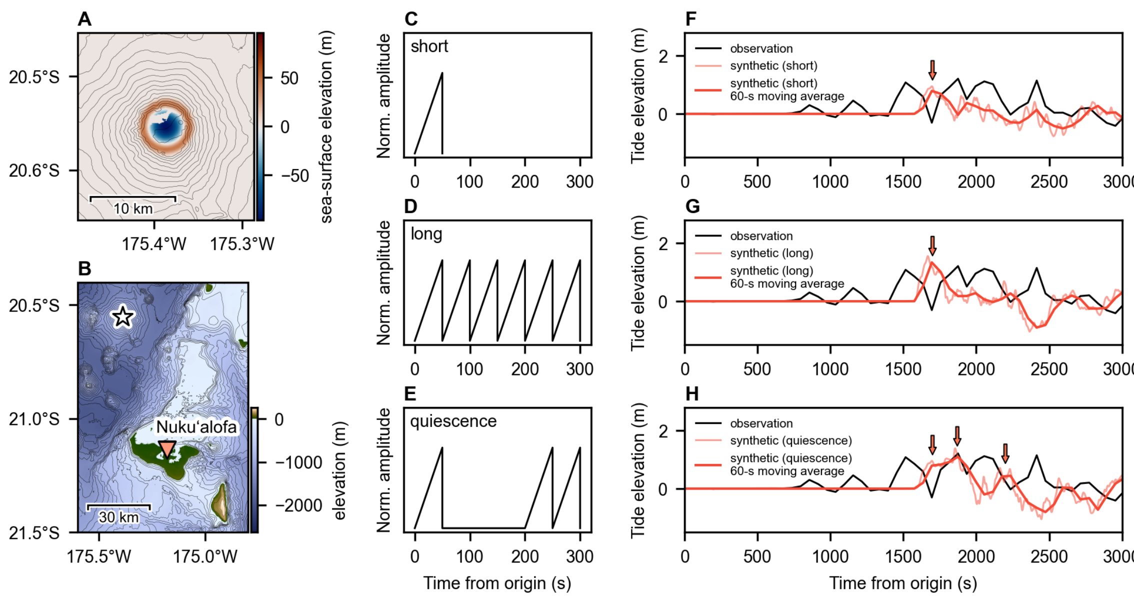

Figure S9: Near-field tsunami simulation. (A) Initial sea-surface displacement of the tsunami source, superimposed on 100-m bathymetric contours. (B) Compiled topo-bathymetry; the star marks Hunga and the inverted triangle marks the Queen Salote Wharf tide gauge, Nuku'alofa. Solid and dashed contours (100-m interval) denote elevations below and above sea level. (C–E) Normalized source-time functions of the three scenarios (*21*). (F–H) Observed tide-gauge record (black) compared with the synthetic waveform (light red) and its 60-s moving average evaluated at the gauge logging times (red) for each scenario. Arrows mark the distinct peaks of the averaged synthetics; only the quiescence scenario produces multiple separated peaks of comparable amplitude, with spacing comparable to the observed sequence.

Table S1: Misfit increase for reduced-component inversions.

Configuration	χ^2 refit	$\Delta\chi^2$ relative to selected (%)	Below threshold?
Full 9 components	1.35×10^4	—	—
ISO + 3 SF (free sign)	1.77×10^4	+31%	No
ISO only (free sign)	2.86×10^4	+111%	No
Deviatoric + 3 SF (free sign)	2.78×10^4	+106%	No
MT only (no SF)	2.51×10^4	+86%	No
SF only (no MT)	3.28×10^4	+143%	No